



Enhancement and suppression of near-field radiative heat transfer in planar many-body systems

Sina Khayam ¹ and Mohammad Ghashami ^{1,2,*}

¹*Mechanical and Materials Engineering Department, University of Nebraska-Lincoln, Lincoln, Nebraska 68588, USA*

²*Mechanical and Industrial Engineering Department, University of Illinois-Chicago, Chicago, Illinois 60607, USA*



(Received 7 May 2024; revised 21 June 2024; accepted 25 June 2024; published 9 July 2024)

This work presents an alternative scheme for modulating near-field radiative heat transfer (NFRHT) within an extended planar many-body system, marking a significant stride in thermal management for micro- and nanodevices. Our approach leverages an adjustable number of interacting bodies, offering a dynamic solution to enhance or suppress NFRHT across diverse configurations. Utilizing the general Green's function approach alongside the scattering matrix method, we establish a Landauer-like formalism, providing a clear, comprehensive framework for calculating NFRHT in many-body systems. This framework adeptly accommodates variations in physical parameters such as layer thickness, separation distance, and material properties, thus facilitating a broad spectrum of many-body planar configurations. Our findings highlight the substantial potential of introducing intermediate layers between traditional two-body systems, enabling additional heat transfer channels and significantly influencing the overall radiative heat flux. By adjusting the relative positions of these layers, the system transitions seamlessly between two-body, three-body, and four-body configurations, offering versatile heat flux modulation. The introduction of artificially engineered materials as intermediate layers further amplifies this effect, showcasing a consistent heat flux enhancement across extended gap distances (d) and thicknesses (t) up to 225 nm, with the maximum amplification of 60% occurring in regions where $t \approx d$. This investigation provides insights into the interactions within complex many-body systems and introduces a practical methodology for precise thermal flux control, paving the way for advancements in nanoscale energy harvesting, photonics, and sensing devices.

DOI: [10.1103/PhysRevB.110.035412](https://doi.org/10.1103/PhysRevB.110.035412)

I. INTRODUCTION

Near-field radiative heat transfer (NFRHT) is a regime arising when the size of the objects and/or their separation distance is comparable to or smaller than the characteristic wavelength [1]. Many studies have demonstrated that NFRHT can exceed Planck's black-body limit thanks to photon tunneling of evanescent modes and surface resonances across the vacuum gap between interacting bodies [2–6]. In addition to high magnitude heat flux, near-field thermal emission can be coherent, quasimonochromatic, and polarized, which has enabled various technologies, including scanning thermal microscopy [7–9], photonics and sensing devices [10–12], nanoscale energy harvesting devices [13–17], and contactless cooling [18]. Additionally, leveraging the unique optical and thermal properties of interacting materials, NFRHT not only offers significant advantages for the thermal management of micro- and nanodevices [19–22] but also plays a crucial role in a wide array of applications where the precise control over the direction and intensity of nanoscale heat transfer is critical [23–27].

The manipulation of NFRHT strongly depends on the number of interacting objects within the system and their characteristics. In a two-body system (i.e., a system containing only two interacting objects), NFRHT has been studied

for various applications such as thermophotovoltaics power generation [14,28–34], thermal rectification [35–40], and non-contact refrigeration [17,41–43]. Further unique behaviors of NFRHT in two-body systems have been proposed using alternative materials and surfaces, including 2D layer structures [44–48], hyperbolic materials [49–53], anisotropic surfaces [51,54,55], multilayers [56–58], nanowires [56,59,60], nanoporous [56,61], and grating patterns [62–66]. While remarkable manipulation of radiative heat transfer has been achieved using the above materials, traditional two-body systems still suffer from inherent limitations due to a constrained number of heat transfer channels available in the transverse wave vector [67,68]. Conversely, in nature and many practical scenarios, it is more common to encounter thermal radiation in systems with more than two objects, making the comprehension of the intrinsic interactions among multiple bodies crucial. To address these complexities, the N -body theory [69,70] was developed to examine heat transport in systems composed of mutually interacting spherical nanoparticles. Subsequent research has focused on creating comprehensive frameworks for calculating NFRHT within more intricate many-body geometries. This includes NFRHT between two particles in the presence of a plate or two plates [71], between spheroidal particles [72], between arbitrary geometries [73–78], and between nanoparticles in the presence of a cylinder [79,80]. However, focusing specifically on planar many-body systems, the calculation of NFRHT initially began by introducing a formalism for nanoscale

*Contact author: ghashami@uic.edu

thermal radiation within a three-body system [81]. This idea was followed by numerous studies exploring the unique inherent mutual interactions within three-body planar systems leading to enhancement or suppression of NFRHT [82,83] and waveguide effect [84]. For instance, it was demonstrated that employing a planar three-body system with an artificially engineered material as an intermediate layer could lead to a notable enhancement in NFRHT between the two sides compared to a two-body counterpart [81].

Subsequent research has demonstrated that three-body systems offer greater potential for nanoscale thermal management compared to two-body configurations, owing to the additional channels (i.e., number of modes) that contribute to the heat transfer [81]. Leveraging these channels, later studies focused on developing innovative thermal management devices, including thermal radiative transistors [85], switches [86,87], logic gates and circuits [88,89], and memories [90]. Furthermore, a variety of techniques for modulating radiative heat flow have emerged, employing strategies such as the use of metal-insulator transition materials [85,86,91–93], the application of magnetic fields to magneto-optical materials [94], the deployment of 2D materials and hyperbolic components for mode hybridization [84,93,95], and the integration of grating or nanoporous structures [96–99]. However, these advancements primarily focus on three-body systems and face challenges in scalability and adaptability to systems involving more bodies, due to the complexities and irreversible modifications required. Hence, there is a pressing need for a versatile approach that can efficiently regulate NFRHT across a broader spectrum of many-body configurations without necessitating significant structural changes.

To address this issue, this work introduces an alternative scheme for modulating NFRHT within an extended planar many-body system featuring an adjustable number of interacting bodies. We employ the general Green's function approach along with the scattering matrix method [100] and rephrase the final expressions into a Landauer-like formalism, establishing a comprehensive framework applicable to a broad spectrum of many-body planar configurations, including our focus on extending the system from two to four components. In this study, we assume the source and sink to be semi-infinite polar dielectrics with constant temperatures. We further assume that two thin layers are initially attached to the source and sink, while they can be freely moved away from those two surfaces. This hypothetical configuration enables us to investigate the change in NFRHT by altering the relative placement of these two layers with respect to the sink and source, exploring the transition from a two-body to a four-body and three-body configuration.

Subsequently, we examine how the introduction of the intermediate body(ies) to a conventional two-body system, resulting in additional contributing heat transfer channels, affects the potential to manipulate overall radiative heat flux. We also explore the influence of physical parameters such as the thickness of layers, relative separation distance, and material properties. Comparing the extended four-body system to the common two- and three-body configurations, we demonstrate the remarkable controllability of the heat flux enabled by introducing intermediate layers. The tuning of heat flux is

accomplished by adjusting the positions of the middle layers relative to each other and to the source and sink slabs. This dynamic adjustment leads to varying amounts of heat flux exchanged between the objects, ranging from a minimum value slightly lower than that of the two-body system to significantly high values. The proposed method introduces opportunities to leverage extended many-body systems for efficient near-field thermal management with minimum structural change. Additionally, it enriches our understanding of the unexplored interactions among objects within complex many-body systems, which are still believed to be elusive and much more complex than those observed in conventional two-body systems.

The remainder of this paper is organized as follows. In Sec. II, we present a description of the physical system under consideration; in Sec. III, we provide the simplified representation of Green's function approach in conjunction with the scattering matrix for the calculation of the NFRHT in many-body planar configurations with isotropic materials and introduce an approach to determine the equilibrium temperature of the intermediate body(ies). Section IV is devoted to a detailed explanation of the proposed framework for the extended many-body system and how it can dynamically transform from a simple two-body system into a more complex configuration. It also includes the analysis of NFRHT in the proposed framework and investigates the potential of such a dynamic system in modulating NFRHT. Finally, our main results are summarized and discussed in Sec. V.

II. PHYSICAL SYSTEM

The schematic representation of the system under study is depicted in Fig. 1. To begin, we consider the NFRHT in a planar two-body system comprising two semi-infinite homogeneous, isotropic, and nonmagnetic parallel slabs, as shown in Fig. 1(a). These slabs are labeled with indices “*h*” and “*c*” representing the hot source and cold sink, respectively, while their temperatures are fixed. Unless otherwise stated, the analysis within this manuscript assumes that both slabs are fabricated from silicon carbide (3C-SiC) where its frequency-dependent dielectric function is modeled using a damped harmonic oscillator [101]:

$$\varepsilon(\omega) = \varepsilon_{\infty} \left(\frac{\omega^2 - \omega_{\text{LO}}^2 + i\gamma\omega}{\omega^2 - \omega_{\text{TO}}^2 + i\gamma\omega} \right), \quad (1)$$

where $\varepsilon_{\infty} = 6.7$ is the high-frequency dielectric constant, $\omega_{\text{LO}} = 1.825 \times 10^{14}$ rad s⁻¹ and $\omega_{\text{TO}} = 1.494 \times 10^{14}$ rad s⁻¹ are the longitudinal and transverse optical phonon frequencies, respectively, and $\gamma = 8.966 \times 10^{11}$ rad s⁻¹ is the damping factor.

Now, to demonstrate the significant potential in modulating heat transfer, we explore the variation of NFRHT by transforming the same classical two-body system to three-body and four-body configurations. To this aim, we conceptualize a hypothetical system wherein two thin layers (with finite thicknesses t_1 and t_2) are initially resting on the two semi-infinite slabs, as shown in Fig. 1(b), while they can freely move and be separated from the slabs. By detaching the two thin layers and approaching them together, the system

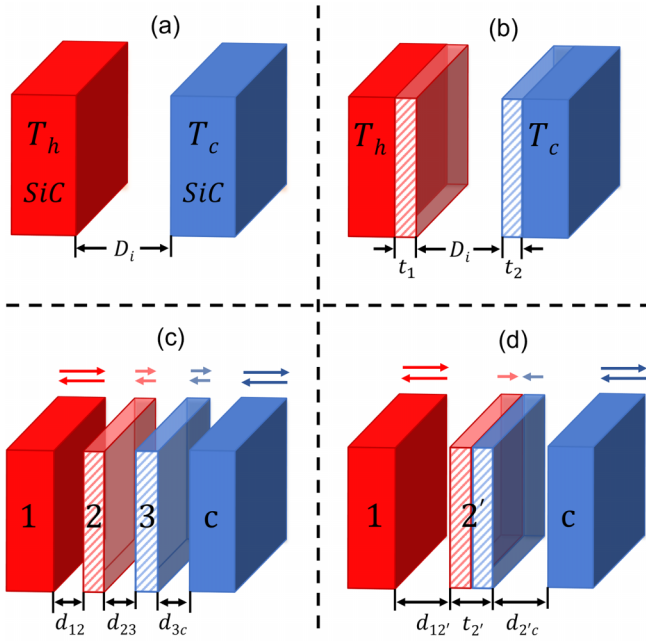


FIG. 1. Schematic illustration of our theoretical system. (a) Initial configuration: The two semi-infinite slabs are separated by a vacuum gap distance of D_i . (b) Hypothetical scenario by assuming two thin layers with thicknesses t_1 and t_2 are resting on the bulk slabs and can be freely moved. (c) Assuming the thin layers (labeled 2 and 3) are separated from the slabs, forming a four-body system. (d) The two thin layers are joined to make an intermediate layer (labeled as 2' with thickness $t_{2'} = t_1 + t_2$), forming a three-body system. In this context, we label the components using the index j ($j = 1, 2, 3$) starting from the hot source, while we keep the label for the cold sink as c .

will transition from its initial two-body state to a four-body configuration and subsequently a three-body setup (when the two thin layers meet in the middle), see Figs. 1(c) and 1(d). In our analysis, we do not consider the effect of Casimir forces between the proximate components to focus on the primary objective of demonstrating NFRHT variation across different system configurations. It is important to recognize that while the configurations suggested by our theoretical model may not yet be easily achievable with existing experimental methods due to technical limitations, the insights gleaned from this study are invaluable. Through this theoretical framework, we illuminate the variations in NFRHT that accompany the system's transition between different configurations, offering a deeper understanding of the underlying physical phenomena. Looking forward, the authors believe that utilizing nanofabrication techniques such as electron beam lithography or focused ion beam milling will enable precise fabrication of thin layers (labeled 2 and 3) with defined thicknesses t_1 and t_2 on bulk slabs. Additionally, effective strategies such as adjusting the thermal expansion of interacting layers to control the distance between hot and cold sources [102,103], employing piezoelectric actuators to precisely manipulate layer positions [43], and fabricating MEMS and NEMS devices with weight load response [104–106], will enable adjustments in extended systems.

III. THEORETICAL FRAMEWORK OF THE EXTENDED MANY-BODY SYSTEM

A. Calculation of NFRHT for an extended many-body system

To begin with, among various methods developed for the calculation of NFRHT between closely spaced objects [81,107,108], we employ the general Green's function approach, suitable for describing the NFRHT in many-body planar configurations made of optically isotropic materials [100]. This method is based on the solution of dyadic Green's functions, where the amplitude of the fields in each body is calculated via a scattering matrix approach. Following this method, the radiative heat flux on the outermost body can be expressed as a sum of evanescent and propagative wave contributions originating from other body(ies). By reformulating the proposed NFRHT representation into a well-known Landauer-like formalism, we provide a comprehensive framework applicable to a wide range of planar many-body systems consisting of homogeneous, isotropic, and nonmagnetic parallel layers. Central to this approach is the derivation of explicit expressions for transmission probabilities. Following the convention for indexing the interacting layers introduced in Fig. 1, the net NFRHT received by the cold sink slab within the extended many-body system, ϕ_c , can be expressed as the summation of the contributions from each layer, $\phi_{i \rightarrow j}$, as follows:

$$\begin{aligned} \phi_c &= \sum_{j \neq c} \phi_{j \rightarrow c} \\ &= \int_{\omega=0}^{\infty} d\omega \int_{-\infty}^{\infty} \frac{d\mathbf{K}_\rho}{8\pi^3} \sum_{j \neq c} [\Theta_j(\omega, T_j) \times \mathcal{T}_{j \rightarrow c}(\mathbf{K}_\rho, \omega) \\ &\quad - \Theta_c(\omega, T_c) \times \mathcal{T}_{c \rightarrow j}(\mathbf{K}_\rho, \omega)], \end{aligned} \quad (2)$$

where index j is considered as 1, 2, or 3 for a two-body, three-body, or four-body system, respectively. $\Theta_j(\omega, T_j) = \hbar\omega / [\exp(\hbar\omega/k_B T_j) - 1]$ is the mean energy of photons with angular frequency ω , $\mathbf{K}_\rho = (k_x, k_y)$ is the component of the wave vector parallel to the interface, and $\mathcal{T}_{c \rightarrow j}$ ($\mathcal{T}_{j \rightarrow c}$) denotes the transmission probability for the thermal photons associated with mode $(\mathbf{K}_\rho, \omega)$ coming from layer c to layer j (layer j to layer c). It is also important to note that due to the reciprocity principle, $\mathcal{T}_{c \rightarrow j} = \mathcal{T}_{j \rightarrow c}$.

Moving forward, the polar coordinate system (ρ, θ, z) is adopted due to the azimuthal symmetry of the problem. Consequently, using the following cartesian coordinate relationships $\mathbf{K}_\rho = k_x \hat{\mathbf{X}} + k_y \hat{\mathbf{Y}}$ and $d\mathbf{K}_\rho = dk_x dk_y$, the transformation of $d\mathbf{K}_\rho$ to the polar coordinate system is performed as

$$\begin{aligned} \int_{-\infty}^{\infty} d\mathbf{K}_\rho &= \int_{-\infty}^{\infty} \int_{-\infty}^{\infty} dk_x dk_y \\ &= \int_{k_\rho=0}^{\infty} \int_{\theta=0}^{2\pi} k_\rho dk_\rho d\theta = 2\pi \int_0^{\infty} k_\rho dk_\rho. \end{aligned} \quad (3)$$

By substituting Eq. (3) into Eq. (2) and assuming a reciprocal system with identical received-transmitted field ratios when exchanging a source and an observer, the final form of

the net NFRHT received by layer c can be expressed as

$$\begin{aligned}\phi_c &= \int_{\omega=0}^{\infty} \phi_{\omega,c} d\omega \\ &= \int_{\omega=0}^{\infty} d\omega \int_{k_\rho=0}^{\infty} \frac{k_\rho dk_\rho}{4\pi^2} \\ &\quad \times \sum_{j \neq c} [\Theta_j(\omega, T_j) - \Theta_c(\omega, T_c)] \times \mathcal{T}_{j \rightarrow c}(k_\rho, \omega),\end{aligned}\quad (4)$$

where transmission probabilities can be defined as

$$\begin{aligned}\mathcal{T}_{j \rightarrow c}(k_\rho, \omega) &= 4k_v^2 \text{Re} \left\{ i\varepsilon_j''(\omega) \int_{z'=z_j}^{z'=z_{j+1}} dz' \right. \\ &\quad \times \left. \begin{aligned} &g_{j_c, \rho\rho}^E(k_\rho, z_c, z', \omega) g_{j_c, \theta\rho}^{H*}(k_\rho, z_c, z', \omega) \\ &+ g_{j_c, \rho z}^E(k_\rho, z_c, z', \omega) g_{j_c, \theta z}^{H*}(k_\rho, z_c, z', \omega) \\ &- g_{j_c, \theta\theta}^E(k_\rho, z_c, z', \omega) g_{j_c, \rho\theta}^{H*}(k_\rho, z_c, z', \omega) \end{aligned} \right\},\end{aligned}\quad (5)$$

with the magnitude of the wave vector in the vacuum defined as $k_v = \omega/c_v$, where c_v is the speed of light in vacuum. The terms $g_{j_c, \alpha\beta}^{E,H}(k_\rho, z_c, z', \omega)$ on the right-hand side of Eq. (5) represent the electric and magnetic Weyl components of the Dyadic Green's functions (DGFs) where α and β are the orthogonal components of a polar coordinate system (i.e., ρ , θ , z). These functions establish the relationship between the fields at a source point z' with frequency ω , located in layer j , to the point in layer c , denoted as z_c , where the radiative heat flux is calculated. Here, $g_{j_c, \rho\rho}^E g_{j_c, \theta\rho}^{H*} + g_{j_c, \rho z}^E g_{j_c, \theta z}^{H*}$ can be seen as a term associated with the transmission probability of the TM-polarized waves, while $g_{j_c, \theta\theta}^E g_{j_c, \rho\theta}^{H*}$ is for TE-polarized waves [100]. It is also important to note that the transmission probabilities inherently rely on the reflection and transmission coefficients through the Weyl components of DGFs and their constitutive field amplitudes of A_c , B_c , C_c , and D_c . The detailed procedure for utilizing the scattering matrix method to obtain field amplitudes necessary for computing DGFs in planar multilayer structures has been slightly modified and outlined in Appendix A to provide an explicit equation for the transmission probability. The Weyl components of the DGFs have also been introduced in Appendix B.

Finally, to derive an explicit equation for the transmission probability, it is necessary to integrate $g_{j_c, \alpha\beta}^E g_{j_c, \alpha\beta}^{H*}$ over z' , which represents the position of the source point within layer j . This process is straightforward in the specific case of a semi-infinite source, since the z' -dependence of the DGF Weyl components can be expressed as [100]

$$\begin{aligned}g_{j_c, \alpha\beta}^E(k_\rho, z_c, z', \omega) g_{j_c, \alpha\beta}^{H*}(k_\rho, z_c, z', \omega) \\ = g_{j_c, \alpha\beta}^E(k_\rho, z_c, \omega) g_{j_c, \alpha\beta}^{H*}(k_\rho, z_c, \omega) e^{2k_{z,j}'' z'}.\end{aligned}\quad (6)$$

As a result, performing analytical integration over z' from $z_j = -\infty$ to $z_{j+1} = 0$ eliminates the dependence of DGFs on z' [see Fig. 13(a) in Appendix B]. Thus, the transmission

probabilities can be obtained as

$$\begin{aligned}\mathcal{T}_{j \rightarrow c}(k_\rho, \omega) \\ = \frac{2k_v^2}{k_{z,j}''} \text{Re} \left\{ i\varepsilon_j''(\omega) \begin{bmatrix} g_{j_c, \rho\rho}^E(k_\rho, z_c, \omega) g_{j_c, \theta\rho}^{H*}(k_\rho, z_c, \omega) \\ + g_{j_c, \rho z}^E(k_\rho, z_c, \omega) g_{j_c, \theta z}^{H*}(k_\rho, z_c, \omega) \\ - g_{j_c, \theta\theta}^E(k_\rho, z_c, \omega) g_{j_c, \rho\theta}^{H*}(k_\rho, z_c, \omega) \end{bmatrix} \right\},\end{aligned}\quad (7)$$

where $\varepsilon_j = \varepsilon_j' + i\varepsilon_j''$ and $k_{z,j} = k_{z,j}' + ik_{z,j}'' = \sqrt{\varepsilon_j k_v^2 - k_\rho^2}$ are defined as the frequency-dependent dielectric function and the z component of the wave vector, both for layer j , respectively. However, in a general case where the source layer has a finite thickness, while it is still feasible to perform analytical integration over z' , this process can be cumbersome; hence, the final expression for the transmission probability in such cases is provided in Appendix B.

B. Determination of the equilibrium temperature of the intermediate body(ies)

Assuming that the outermost slabs are kept at constant temperatures T_1 and T_c , the intermediate layers achieve steady state in the absence of external bias, settling at new equilibrium temperatures denoted as T_j ($j = 2'$ or $2, 3$). The equilibrium temperature of the intermediate layers is assumed to be uniform across the thin layers and can be determined by applying energy balance, ensuring that the net energy flux to and from layer j is zero [81,96,109]. By inspecting Figs. 1(c) and 1(d), the equilibrium temperature of the described layers is determined from

$$\begin{cases} \phi_{2,\text{net}} = \phi_{1 \rightarrow 2} + \phi_{3 \rightarrow 2} + \phi_{c \rightarrow 2} = 0 & \text{for four-body system,} \\ \phi_{3,\text{net}} = \phi_{1 \rightarrow 3} + \phi_{2 \rightarrow 3} + \phi_{c \rightarrow 3} = 0 & \\ \phi_{2',\text{net}} = \phi_{1 \rightarrow 2'} + \phi_{c \rightarrow 2'} = 0 & \text{for three-body system,} \end{cases}\quad (8)$$

where considering the finite thickness of the intermediate slab of j , the radiative heat flux absorbed by this layer, denoted as $\phi_{i \rightarrow j}$, is determined by calculating the difference between the flux received by its left and right interfaces. To this end, the contribution of each layer in the net radiative heat flux received by body j at interface $z = z_j^\pm$ can be expressed as

$$\begin{aligned}\phi_{i \rightarrow j}(z_j^\pm) &= \int_{\omega=0}^{\infty} d\omega \int_{k_\rho=0}^{\infty} \frac{k_\rho dk_\rho}{4\pi^2} [\Theta_i(\omega, T_i) - \Theta_j(\omega, T_j)] \\ &\quad \times \mathcal{T}_{i \rightarrow j}(k_\rho, \omega, z_j^\pm).\end{aligned}\quad (9)$$

However, by plotting the spectral heat flux $\phi_{\omega,c}$ when all bodies are of SiC [which supports surface phonon polaritons (SPhPs)], we can observe a quasimonochromatic heat-flux spectrum, as depicted in Fig. 2. This observation allows for a simplified approach to establishing the equilibrium temperature of the intermediate layer(s) by solving the energy balance [i.e., Eqs. (8) and (9)] exclusively at the SPhP frequency of SiC, denoted as $\omega_{\text{SPhP}} = 1.786 \times 10^{14}$ rad s^{-1} [101]. Employing this approach within the proposed extended many-body

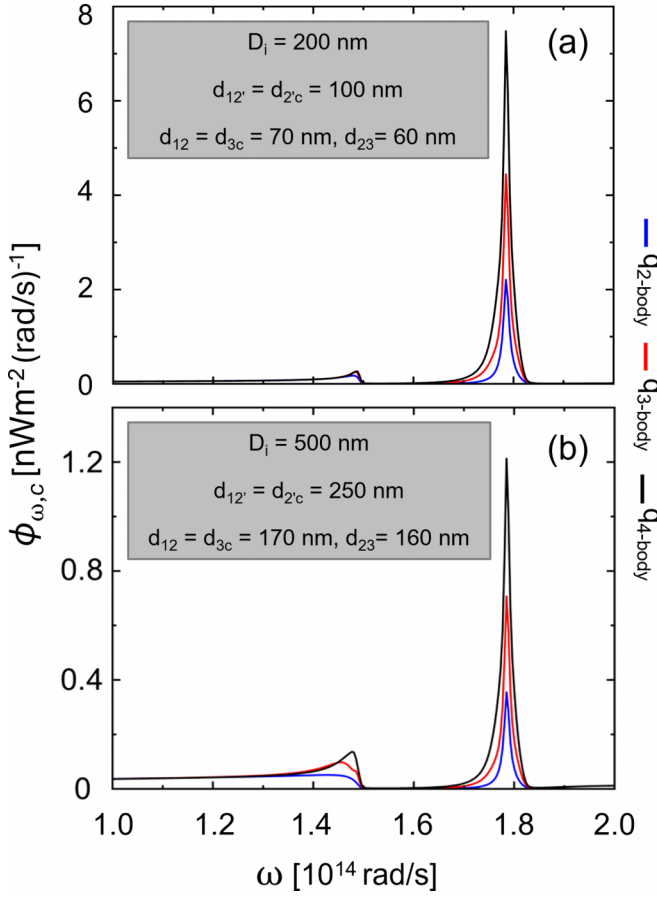


FIG. 2. Spectral heat fluxes $\phi_{\omega,c}$ within two-, three-, and four-body systems for two different initial gap distances: D_i of 200 and 500 nm while the temperature of the hot and cold slabs for both cases are set at $T_1 = 400$ K and $T_c = 300$ K, respectively. For each case, the specified values of t_1, t_2 have been used where $t_{2'} = t_1 + t_2$. (a) In the first case, the values are chosen as $t_1 = t_2 = 100$ nm. (b) For the second case, the assigned values are $t_1 = t_2 = 250$ nm.

system composed of SiC, with the hot and cold slabs set at $T_1 = 400$ K and $T_c = 300$ K, respectively, results in the intermediate body stabilizing at $T_2 = 357.1$ K for the three-body configuration. In this configuration, the thickness of the intermediate layer is $t_{2'} = 200$ nm, with gap distances of $d_{12'} = d_{2'c} = 100$ nm. Similarly, for a four-body configuration with equal thicknesses of $t_1 = t_2 = 100$ nm and gap distances of $d_{12} = d_{3c} = 70$ nm and $d_{23} = 60$ nm, the middle layers achieve equilibrium temperatures of $T_2 = 366.4$ K and $T_3 = 347.4$ K, respectively. The obtained equilibrium temperatures ensure a zero net heat flux absorbed by the intermediate layer(s) in the proposed extended system.

IV. MANIPULATION OF HEAT FLUX IN THE EXTENDED MANY-BODY SYSTEM

To investigate the influence of varying the relative positions of interacting layers within an extended many-body system on radiative heat flux, we examine two specific scenarios. In the first scenario, the system transitions from a two-body to a four-body configuration by holding the outer semi-infinite slabs stationary while progressively moving the two thin lay-

ers closer together. This process continues until the layers converge, effectively creating a three-body system. The second scenario contrasts by keeping the thin layers fixed while the semi-infinite slabs are relocated outwards, thereby maintaining a four-body configuration. This methodical adjustment in both scenarios facilitates a detailed investigation into the effect of spatial rearrangements on the radiative heat flux across the system.

A. First scenario: Inward movement of inner layers

We begin our investigation by assessing the total radiative heat flux received by slab c , focusing on the effect of varying the separation distance between the middle thin layers. During this analysis, the two outer slabs remain stationary, facilitating the expansion from a two-body system to more complex configurations, as shown in Figs. 3(a) and 3(b). To this end, the temperatures of slab 1 and slab c are set at $T_1 = 400$ K and $T_c = 300$ K, respectively. The initial gap distance in the two-body system is specified as $D_i = 200$ nm, and the thickness of the two thin layers is selected as $t_1 = t_2 = t = 100$ nm. In this scenario, the sum of all gap distances between layers remains constant. For instance, in the case of a four-body system, $D = d_{12} + d_{23} + d_{3c} + 2t$, where $d_{12}, d_{23},$ and d_{3c} are the distances between adjacent layers and t is the thickness of each thin layer. Note that $d_{12} + d_{23} + d_{3c} = D_i$, meaning that $D - D_i = 2t$. Conversely, for a three-body system, $D = d_{12'} + d_{2'c} + 2t = D_i + 2t$, where the merged middle layer is represented by $2'$. We will focus our study on the symmetric configurations where the gaps between the thin layers and the outer slabs are equal, i.e., $d_{12} = d_{3c} = d$, with d varying from 10 to 90 nm within a four-body system. For the transitioned three-body system, the distances transform to $d_{12'} = d_{2'c} = (D - 2t)/2$, reflecting the merger of the two thin layers into a single entity. It is also important to reiterate that the equilibrium temperatures of the intermediate layers are determined through the energy balance analysis. This ensures a rigorous determination of thermal equilibria consistent with the system's configuration and spacing adjustments.

Figure 3(c) demonstrates the total heat flux ϕ_c , as a function of the gap distance d , where $d = 0$ and $d = 100$ nm correspond to two-body and three-body systems, respectively. It should be noted that the intervals between $d = 0$ nm to $d = 10$ nm and from $d = 90$ nm to $d = 100$ nm are highlighted as transition zones, where the system undergoes a change in the number of interacting layers. We intentionally chose separation increments of 10 nm to confidently apply the fluctuation-dissipation theorem in our calculations and to avoid nonlocal effects and the necessity for quantum corrections. This selection necessitates that the thin layers move in steps of 10 nm to transition from a two-body system to a four-body and then a three-body configuration while remaining within the valid application range of the theorem.

Initially, as the thin layers start to separate from the semi-infinite slabs, there is a marked increase in heat flux. This rise, however, is followed by a decrease as the layers continue to move apart from the slabs, eventually stabilizing into a plateau for the three-body system configuration, which slightly exceeds the heat flux levels of the original two-body system. This phenomenon can be attributed to the coupling

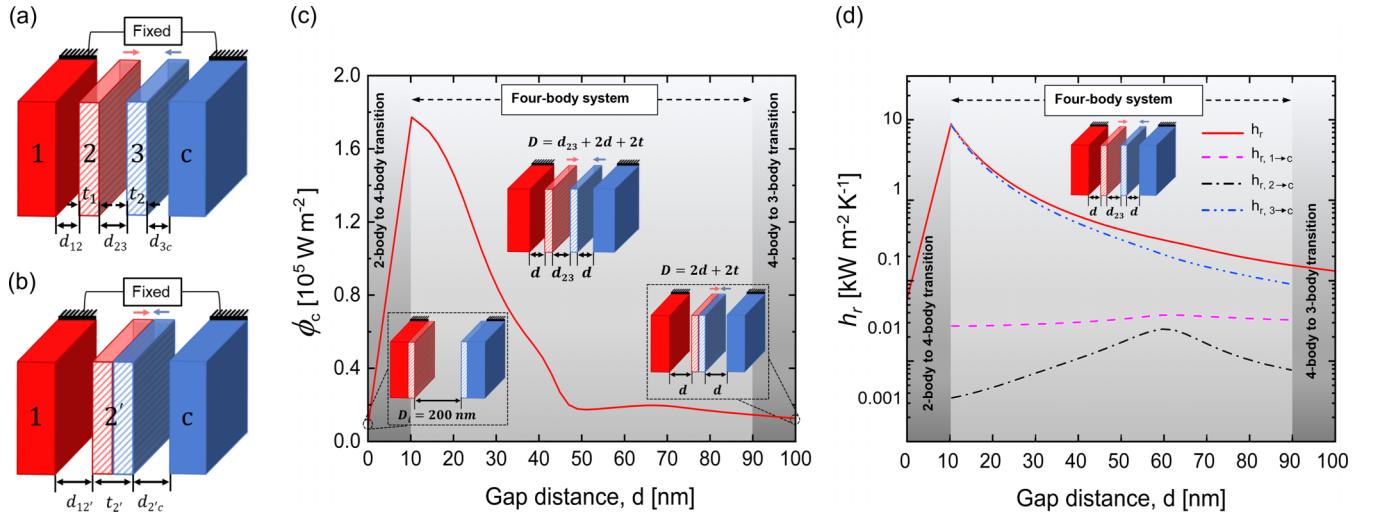


FIG. 3. Schematic of inward movement of the thin intermediate layers. (a) The system transforms from the initial two-body to a four-body configuration through the described adjustment. (b) As the thin layers keep approaching, they eventually combine, giving rise to a three-body system with $t_{2'} = t_1 + t_2$. (c) Total radiative heat flux as a function of vacuum gap distance within the extended many-body system with $t = 100$ nm: Transitioning from two-body to four-body and finally to three-body configurations through inward movements of the thin layers. (d) Heat transfer coefficient for an extended many-body system with $t = 100$ nm and $T_c = 300$ K. For the two-body setup, this coefficient is represented as $h_{r,1 \rightarrow c}$; for the three-body arrangement, it is $h_{r,1 \rightarrow c} + h_{r,2' \rightarrow c}$; and for the four-body configuration, it is $h_{r,1 \rightarrow c} + h_{r,2 \rightarrow c} + h_{r,3 \rightarrow c}$.

of hybridized modes within the many-body system as the thin layers are separated. In the context of thin film layers, SPhP modes manifest on both interfaces, offering a richer mode spectrum than that available to semi-infinite slabs. Thus, in a four-body system configuration with narrow gaps (d), these additional channels contribute to a sharp increase in heat flux compared to a two-body system. As the gap widens, the contribution of these modes gradually lessens, culminating in a plateau that mirrors the heat flux characteristics of a simpler two-body system.

This observation can be verified by examining how the heat flux coefficient changes with varying the gap distance. For simplicity, it is assumed that the temperature differences within the system are sufficiently small (i.e., $|T_j - T_c| \ll \min\{T_1, \dots, T_c\}$), permitting a linearization of Θ . Under this assumption, the net heat flux equation can be linearized by introducing the heat transfer coefficient h_r as [110]

$$\phi_c \simeq \sum_{j \neq c} h_{r,j \rightarrow c} (T_j - T_c), \quad (10)$$

with $T_j = T_c + \Delta T_{j,c}$ and $h_{r,j \rightarrow c}$ defined as [94]

$$\begin{aligned} h_{r,j \rightarrow c} &= \lim_{\Delta T_{j,c} \rightarrow 0} \frac{\phi_{j \rightarrow c}}{\Delta T_{j,c}} \\ &= \int_{\omega=0}^{\infty} d\omega \int_{k_\rho=0}^{\infty} \frac{k_\rho dk_\rho}{4\pi^2} \\ &\quad \times \left[\frac{\partial \Theta_c(\omega, T_c)}{\partial T_c} \times \mathcal{T}_{j \rightarrow c}(k_\rho, \omega) \right]. \end{aligned} \quad (11)$$

The overall heat transfer coefficient, h_r , depicted in Fig. 3(d), demonstrates the effects of varying gap distances (d) while keeping the thicknesses of the layers constant ($t_1 = t_2 = 100$ nm). Notably, h_r significantly increases as the

system transitions from a two-body to a four-body configuration, followed by a gradual decrease as the vacuum gap widens. This trend highlights the significant potential of the explored mechanism for modulating near-field thermal transfer with minimal structural changes. Additionally, the heat transfer coefficient magnitudes for the first ($h_{r,1 \rightarrow c}$) and second layers ($h_{r,2 \rightarrow c}$) are relatively insignificant compared to the third layer ($h_{r,3 \rightarrow c}$), which is expected due to its closer proximity to the receiver, enhancing the coupling between them.

To better understand the impact of expanding a two-body system on heat flux, we analyze the transmission probability at the surface phonon polariton frequency ($\omega = \omega_{\text{SPhP}}$), as a function of the dimensionless wave vector $c_v k_\rho / \omega_{\text{SPhP}}$ and thickness t across various gap distances. This approach helps to unravel the dynamics within systems comprising different numbers of interacting bodies. In our study, the effective transmission probabilities for the three-body and four-body systems are characterized as $\mathcal{T}_3 = (\mathcal{T}_{1 \rightarrow c} + \mathcal{T}_{2 \rightarrow c})/2$ and $\mathcal{T}_4 = (\mathcal{T}_{1 \rightarrow c} + \mathcal{T}_{2 \rightarrow c} + \mathcal{T}_{3 \rightarrow c})/3$, respectively. It is noteworthy that our analysis exclusively considers TM polarization, which is the primary contributor to heat transfer. Furthermore, we focus on symmetric configurations, where the gap distances between the thin layers and the outer slabs are maintained equal, i.e., for the three-body system $d_{12'} = d_{2'c} = d$ and for the four-body system $d_{12} = d_{3c} = d$, as illustrated in Figs. 3(a) and 3(b).

Figure 4 illustrates the transmission probability of a two-body system with an initial gap size of $D_i = 200$ nm, compared against its three-body and four-body counterparts across various gap distances (d), while layer thickness (t) varies from 10 to 300 nm. Observations from Figs. 4(a) and 4(b) reveal a considerable broadening of the transmission probability's wave-vector range in the four-body system, extending the cutoff beyond 800. However, when the layer

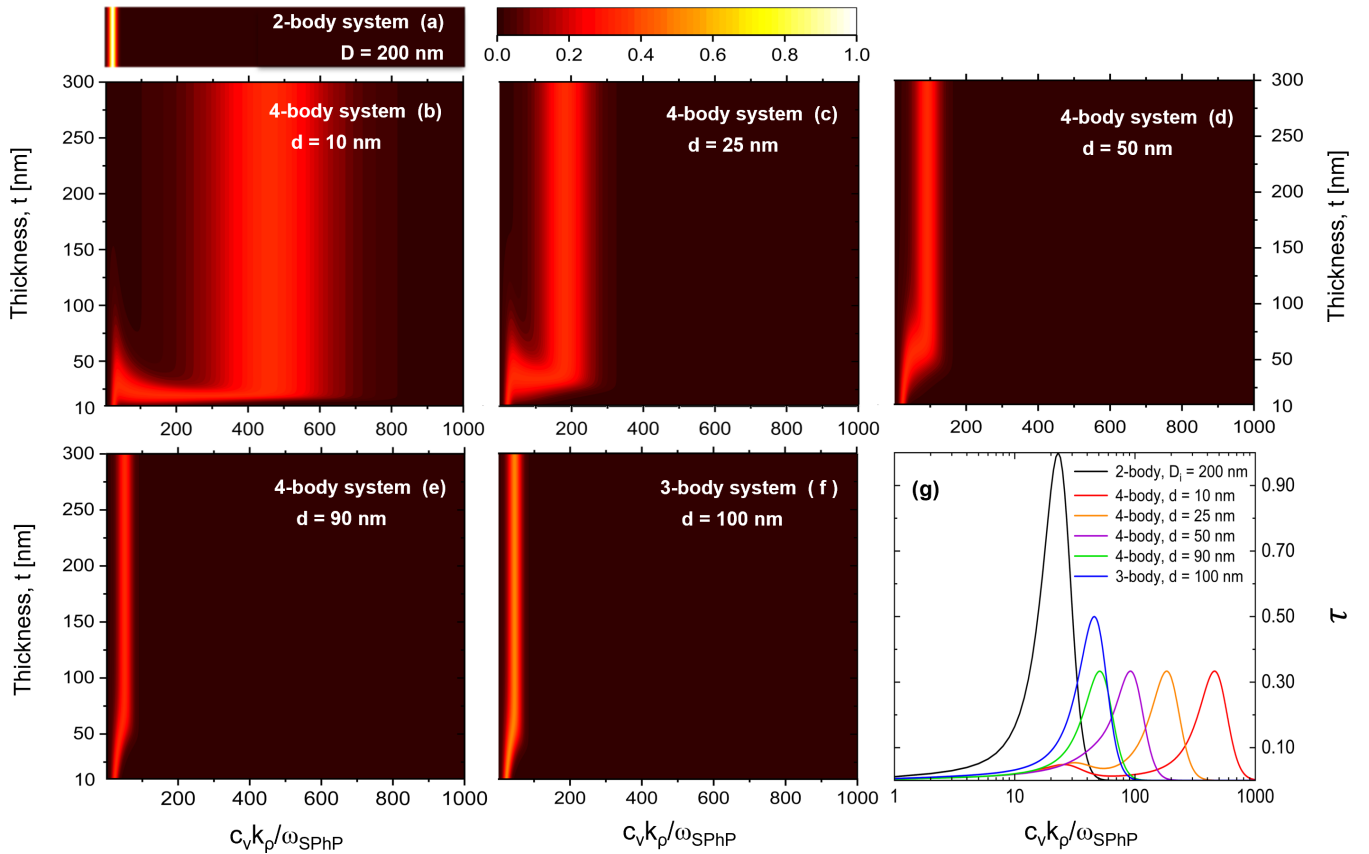


FIG. 4. Transmission probabilities at the $\omega = \omega_{\text{SPHP}}$ of the (a) two-body system \mathcal{T}_2 with an initial gap distance of $D_i = 200$ nm, compared to that of a four-body system \mathcal{T}_4 with (b) $d = 10$ nm, (c) $d = 25$ nm, (d) $d = 50$ nm, (e) $d = 90$ nm, and (f) three-body system \mathcal{T}_3 with $d = 100$ nm. It should be noted that the distances between the thin layers and the outer slabs are assumed equal (i.e., $d_{12} = d_{3c} = d$ for the three-body system and $d_{12} = d_{3c} = d$ for the four-body system). (g) The relative shift in the transmission probability is observed across different configurations of the extended many-body system. Here, the thickness is fixed at $t = 100$ nm for the intermediate layers.

thickness t is much larger than d (i.e., $t \gg d$), the transmission probability of the four-body system becomes independent of thickness, suggesting the intermediate layers effectively behave as semi-infinite slabs. As the gap distances increase, the wave vector's cutoff value decreases, diminishing the long-range wave-vector dependency of transmission probability, as seen in Figs. 4(c) and 4(d). Eventually, at $d = 90$ nm, as shown in Fig. 4(e), the transmission probability closely aligns with that of a three-body [Fig. 4(f)], albeit at a lower magnitude. Despite this difference in the magnitude, we observed a comparable heat flux for these two cases in Fig. 3(c). This phenomenon is explained by the balancing effect of temperature differences between the setups. Specifically, while the transmission probability is lower in the four-body system compared to the three-body, the greater temperature difference between the intermediate layers and the cold slab in the four-body setup compensates for this. Consequently, the multiplication of transmission probabilities and temperature gradients yields similar heat fluxes for both scenarios, demonstrating the complex interplay between structural geometry and thermal dynamics in many-body systems.

Figure 4(g) illustrates the relative shift in the position of the transmission probability peaks for different configurations of the extended many-body system, along with their respective cutoff values when the thickness of the intermediate

layers is fixed at $t = 100$ nm. These observations substantiate the pronounced increase in heat flux as the system transitions from a two-body to a four-body configuration. This increase is attributed to a significant widening in the effective wave-vector range, despite the higher magnitudes observed in the two-body system. Consequently, while the transmission probability magnitude in a two-body system exceeds that of a four-body, its concentration within a narrow wave-vector range results in a comparatively lower heat flux than that seen in the four-body setup. Subsequently, as the gap distance d continues to increase, the transmission probability of a four-body system experiences a relative shift as the cutoff values gradually decrease, eventually reaching a level similar to that of a three-body system.

To enrich our understanding of the dynamics within the proposed extended many-body system, it is important to examine how variations in the thickness (t) of the intermediate layers and their gap distance from the semi-infinite slabs (d) impact total heat flux. To achieve this, we calculate the ratio of total heat flux in the four-body configuration to that in the two-body setup, denoted as $\phi_{4b}(d, t) / \phi_{2b}(D_i)$, where the initial gap distance is defined as $D_i = 200$ nm. Figure 5 illustrates the overall heat flux enhancement across a range of thicknesses from 10 to 100 nm, while varying the gap distance $d_{12} = d_{3c} = d$ from 10 to 95 nm. This range is

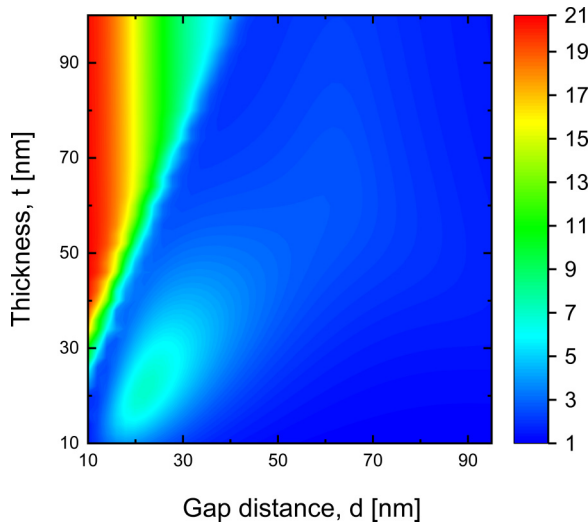


FIG. 5. Heat flux amplification of a four-body system with respect to the two-body setup, $\phi_{4b}(d, t)/\phi_{2b}(D_i)$, as a function of the gap distance d and thickness t for inward movement.

deliberately selected to maintain a minimum gap of 10 nm, essential for facilitating transitions between two-body and four-body configurations. Figure 5 highlights the proposed extended many-body system's ability to modulate heat flux, demonstrating an amplification factor that varies from a baseline of 1 for large gap distances to a peak of approximately

21. This maximum amplification is attained in regions where $10 < d < 20$ nm and $35 < t < 100$ nm. Furthermore, it is evident that up to $d = 40$ nm, the total heat flux received by slab c is attributed to the four-body effect involving all bodies and increases with thickness.

To deepen our comprehension regarding how variations in gap distance and layer thickness affect heat flux amplification, we delve into the analysis of effective transmission probabilities in a four-body system (\mathcal{T}_4) and its constituent components (i.e., $\mathcal{T}_{1 \rightarrow 4}$, $\mathcal{T}_{2 \rightarrow 4}$, and $\mathcal{T}_{3 \rightarrow 4}$). Figure 6 illustrates this analysis across two gap distances, 20 and 70 nm, each evaluated under three thickness conditions: 10, 50, and 100 nm. In the first series of plots ($d = 20$ nm), as thickness increases, we notice changes in both the shape and positioning of the transmission probability peaks for individual layers. These changes boost the system's overall effective transmission probability (\mathcal{T}_4) from $t = 10$ nm to larger thicknesses. Such an enhancement aligns with the observed variations in the amplification factor at $d = 20$ nm with increasing thickness, as highlighted in Fig. 5. In contrast, the second series of plots reveals that while adjustments in thickness modify the transmission probability magnitudes of each contributing layer ($\mathcal{T}_{1 \rightarrow 4}$, $\mathcal{T}_{2 \rightarrow 4}$, and $\mathcal{T}_{3 \rightarrow 4}$), the collective effective transmission probability (\mathcal{T}_4) of the four-body system remains largely unaffected. This observation helps explain the negligible impact of thickness variations on the amplification factor for regions where $d > 40$ nm in Fig. 5. Notably, an enhancement in the local amplification factor is observed in

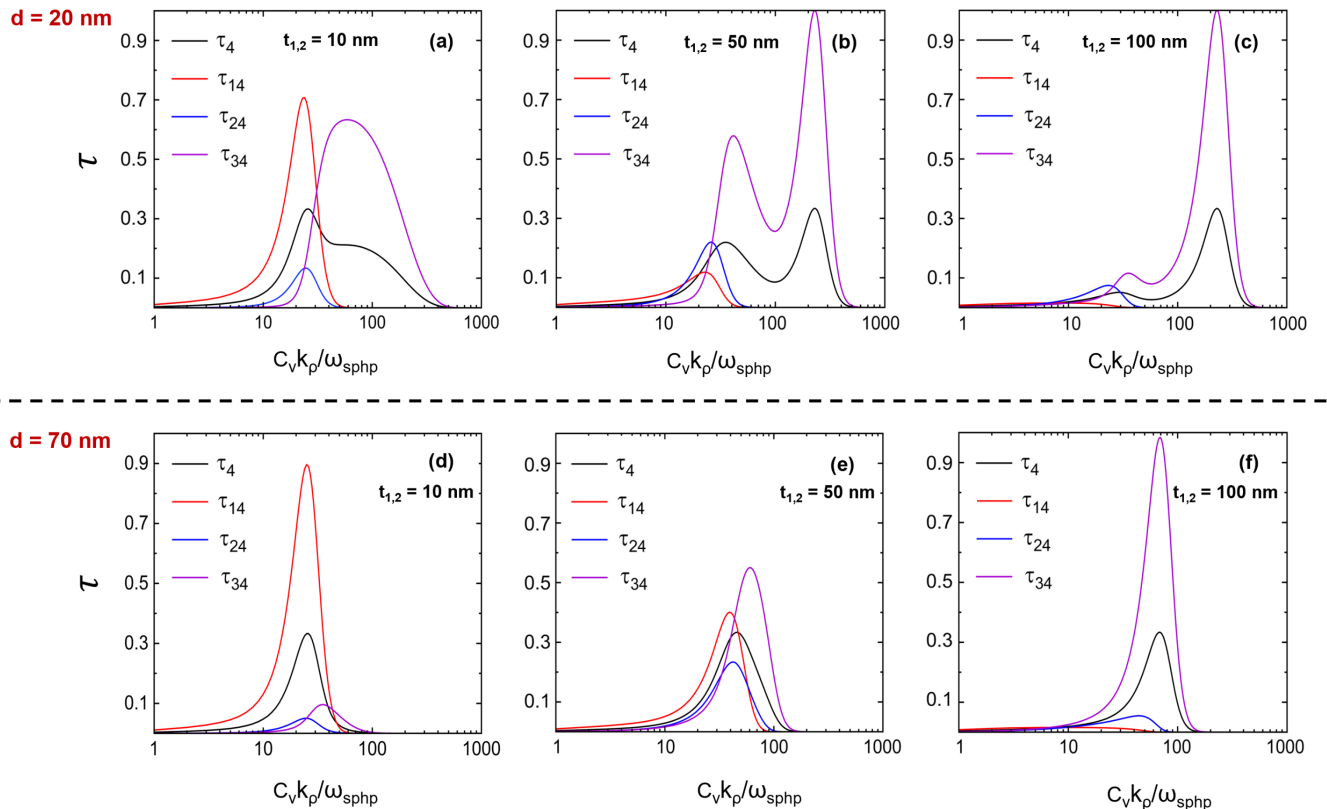


FIG. 6. Effective transmission probability of a four-body system (\mathcal{T}_4) and its individual layer contributions (i.e., $\mathcal{T}_{1 \rightarrow 4}$, $\mathcal{T}_{2 \rightarrow 4}$, and $\mathcal{T}_{3 \rightarrow 4}$). (a)–(c) $d = 20$ nm while $t = 10$ nm, $t = 50$ nm, and $t = 100$ nm, respectively. (d)–(f) $d = 70$ nm while $t = 10$ nm, $t = 50$ nm, and $t = 100$ nm, respectively.

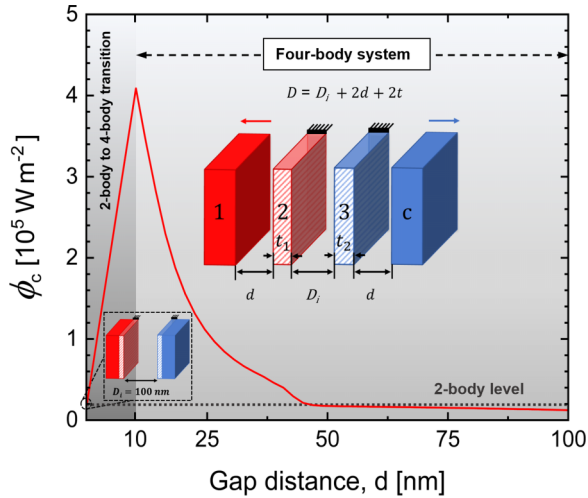


FIG. 7. Total radiative heat flux as a function of gap distance d within an extended many-body system with $t = 100$ nm, capable of transitioning between two-body and four-body configurations during outward movement.

areas where the gap distance and thickness are equivalent ($d = t$), particularly up to 30 nm. This finding resonates with prior research on three-body systems, which also assessed heat flux amplification compared to two-body setups, thus validating the coherence of our observations with established literature [81].

B. Second scenario: Outward movement of semi-infinite slabs

In this section, we focus on the effects of expanding a two-body system into a four-body configuration by moving the outer semi-infinite slabs outwardly. This investigation begins with an initial gap distance of $D_i = 100$ nm for the conventional two-body setup. Unlike the inward adjustment scenario previously discussed, here, the intermediate layers remain stationary, as illustrated in the inset of Fig. 7. Here, the temperatures for slab 1 and slab c are maintained at $T_1 = 400$ K and $T_c = 300$ K, respectively, while the equilibrium temperature of the middle layers is determined through the energy balance analysis. The thickness of each intermediate layer is fixed at $t = 100$ nm. In this outward extension scenario, we focus on symmetric cases where the gap distances between the thin layers and the outer slabs are identical ($d_{12} = d_{3c} = d$). This leads to a total gap distance for a four-body configuration expressed as $D = D_i + 2d + 2t$.

Figure 7 depicts the variation of the total heat flux received by slab c across various gap distances within the extended many-body system, transitioning between two-body and four-body configurations. Similar to the first scenario, a significant rise in the total heat flux occurs once the outer slabs are separated from the inner layers, forming a four-body system. This initial surge in heat flux eventually tapers off, leading to a distinct suppression effect in regions where $d \geq 45$ nm. Here, the heat flux within the four-body system falls below that of the original two-body setup. As discussed below, this observation can be attributed to the interaction of SPhP modes, which are present on both sides of the thin layers, whereas in the semi-infinite slab, they manifest only on one

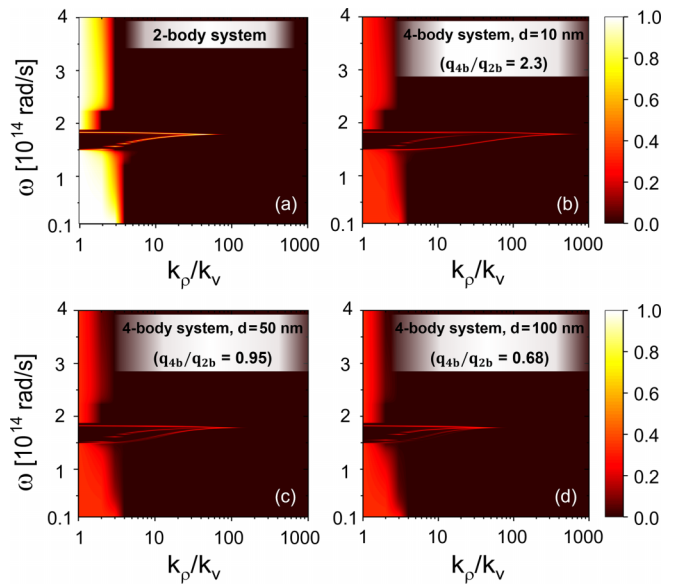


FIG. 8. Examining the effect of increasing gap distance on the transmission probability \mathcal{T} of an extended many-body system with $t = 100$ nm during outward movement. (a) Two-body system with an initial gap distance of $D_i = 100$ nm. (b) Four-body system with $d = 10$ nm. (c) Four-body system with $d = 50$ nm. (d) Four-body system with $d = 100$ nm.

side. The coupling of these SPhP modes between the thin films and the bulk layers initially enhances heat transfer. However, as the gap between layers increases, this coupled effect wanes, leading to the observed reduction in heat flux. Ultimately, as d continues to increase, the four-body system yields a smaller heat flux compared to the two-body configuration. Contrary to the first scenario, which consistently showcased an enhancement in heat flux, this scenario reveals a more complex behavior, exhibiting both enhancement and suppression effects depending on the gap distances. This dual behavior demonstrates the capability to finely adjust near-field radiative heat flux in many-body systems, highlighting the nuanced potential of our proposed modulation mechanism.

To further understand the enhancement and suppression patterns, we analyze the transmission probabilities for each specified gap distance, as shown in Fig. 8. In the two-body configuration, the cutoff value of the normalized wave vector is limited to 100 at the SPhP resonance frequency of SiC. However, in the four-body configuration with $d = 10$ nm, the cutoff value escalates beyond 800 due to the hybridization of surface modes between the thin films and the bulk slabs, resulting in an amplification factor of 2.3; see Figs. 8(a) and 8(b). As the gap distance widens, the cutoff values begin to mirror those of the two-body configuration, signaling a reduction in surface mode hybridization. Consequently, the transmission probabilities drop below those observed in two-body, leading to amplification factors of 0.95 and 0.68 for gap distances $d = 50$ nm and $d = 100$ nm, respectively. This suppression is evident in Figs. 8(c) and 8(d), depicting the nuanced relationship between gap distance, surface mode interactions, and their collective impact on heat flux modulation within the system.

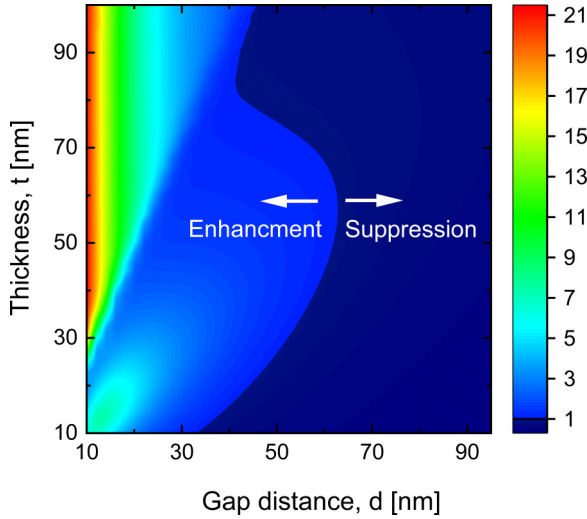


FIG. 9. Heat flux amplification $\phi_{4b}(d, t)/\phi_{2b}(D_i)$ as a function of gap distance d and thickness t for outward movement with an initial gap distance of $D_i = 100$ nm.

We further investigate the impact of varying the thickness of the intermediate layers on the total heat flux amplification factor, as illustrated in Fig. 9. Specifically, we focus on identifying the transition between regions of enhancement and suppression as delineated by the critical amplification factor of 1. At very small gap distances, the outward scenario mirrors the behavior observed in the inward situation, characterized by a substantial increase in heat flux reaching an amplification factor of 21. However, as the gap distance increases, we observe a descending trajectory in the amplification factor, ultimately dipping below 1 (as depicted by the dark blue region in Fig. 9). This trend underscores the versatility of the proposed modulation mechanism, demonstrating its capacity to either enhance or reduce near-field radiative heat flux in many-body systems. Such adaptability highlights the potential of strategic layer and gap distance adjustments in tailoring thermal radiation properties for various applications, offering a nuanced control over heat transfer processes in complex configurations.

C. Special case: Long-range enhancement of NFRHT via artificially engineered material

Until now, we have observed a significant increase in the heat flux within the proposed extended many-body system when dealing with relatively small gap distances. However, for larger gap distances, the amplification factor approaches unity in the first scenario or decreases in the second scenario. This suggests that with larger gap distances, we either maintain the same heat flux as in a two-body system or experience a reduction in heat flux. This observation can change dramatically if we use an artificially engineered material for the intermediate layers to enhance coupling between the phonon polariton modes of SiC. To this aim, we adopt the suggested engineered material introduced in Ref. [81], utilizing it as the intermediate layers within our expanded many-body system, with the dielectric function defined as

$$\varepsilon(\omega) = 1 - \frac{\omega_p^2}{\omega^2 + i\omega\gamma_p}, \quad (12)$$

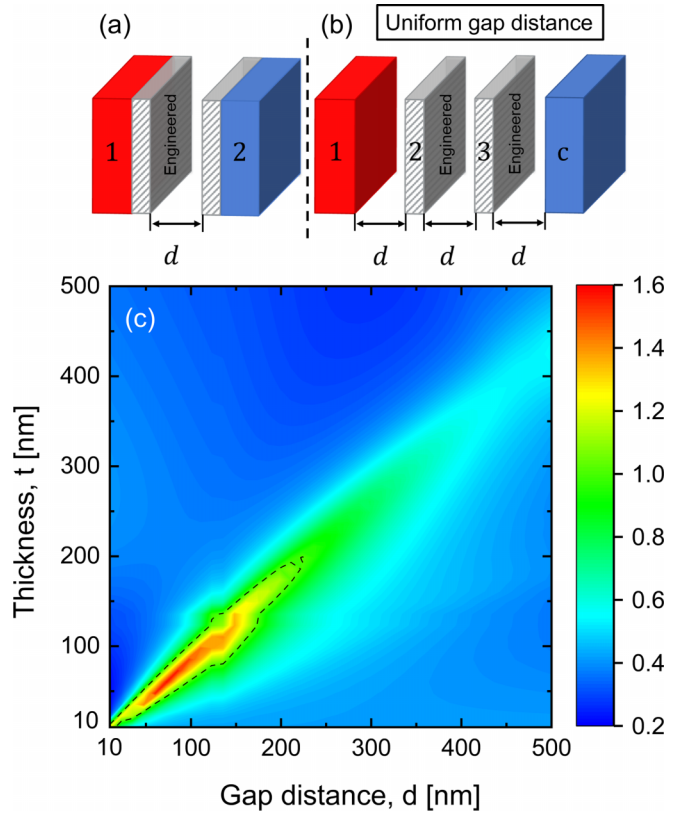


FIG. 10. (a) Schematic illustration of the initial two-body system constructed with two intermediate layers of engineered materials resting on the semi-infinite SiC slabs while the gap is d . (b) Schematic of a four-body system with uniform gap distances between all bodies. (c) Heat flux amplification $\phi_{4b}(d, t)/\phi_{2b}(d)$ as a function of gap distance (d) and thickness (t). The area marked by the dashed line indicates the region where the amplification factor exceeds one.

where ω_p and γ_p are the plasma frequency and the relaxation rate, respectively. By setting the plasma frequency to $\omega_p = \sqrt{2} \omega_{\text{SPhP}}$, we align the engineered material's surface plasmon polariton mode frequency with that of SiC, based on the Drude model's predictions. The relaxation rate is also chosen as $\gamma_p = 10^{-3} \omega_p$, ensuring optimal enhancement of mode coupling.

To evaluate the effectiveness of the engineered material in enhancing heat transfer at larger gap distances, we examine an extended many-body scenario where all the gap distances are identical and equal to that of the two-body system, as depicted in Figs. 10(a) and 10(b). It is assumed that all layers can move freely, with the only constraint that all the separation distances remain equal. Figure 10(c) shows the heat flux amplification in the many-body system shown in Fig. 10(b) compared to that of the two-body shown in Fig. 10(a), as a function of gap distance (d) and layer thickness (t). This figure clearly demonstrates a consistent amplification of heat flux, even for relatively larger gap distances up to 225 nm, while the maximum amplification factor of 1.6 occurs in regions with $t \simeq d$. This outcome suggests a long-range enhancement of near-field radiative heat transfer, a stark contrast to the second scenario where amplification was confined to $d < 60$ nm. The assumption of uniform gap distances within the four-body

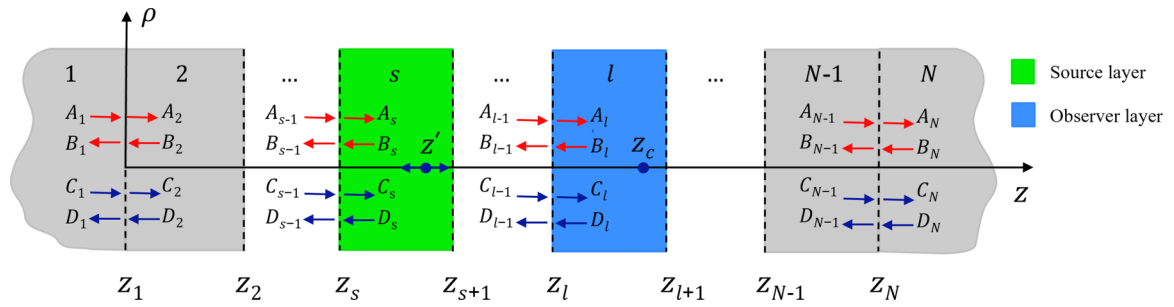


FIG. 11. Field patterns in a multilayer configuration where the point source Z' in layer s emits in both forward (z -positive) and backward (z -negative) directions. The receiver point (Z_c) is assumed in layer c , where the radiative heat flux is calculated.

system in this scenario underscores the efficacy of incorporating an engineered material in significantly enhancing heat flux. That is, this system not only sustains an increased heat flux but also supports expanding the gap distance by up to threefold, extending to $d = 225$ nm. Such an achievement demonstrates considerable potential for practical implementations, showcasing the engineered material's capability to facilitate long-range NFRHT enhancements in many-body configurations.

V. CONCLUSIONS

In this study, we presented an alternative method for modulating near-field radiative heat transfer (NFRHT) through an extended many-body system capable of adjusting the number of interacting bodies. Our approach, grounded in the general Green's function and the scattering matrix methods, yielded explicit expressions within a Landauer-like formalism, offering a versatile framework for various planar many-body configurations. Our findings revealed that in scenarios where outer (semi-infinite) slabs are stationary, separating intermediate layers from the slabs results in a significant initial increase in heat flux within a four-body configuration, followed by a decline, eventually reaching a plateau as the system transitions to a three-body setup. This transition enhances heat flux, with the amplification factor ranging from 21 at minimal gap distances to just over 1 at larger gaps. Conversely, when the intermediate layers remain fixed while outer slabs are adjusted, we observe a similar initial amplification, which diminishes as the gap distance increases, ultimately falling below 1 and indicating suppression of NFRHT. This underscores the proposed system's capability to precisely adjust NFRHT within many-body configurations through minimal structural changes. Additionally, employing artificially engineered materials as intermediate layers while maintaining uniform gap distances, consistently amplified heat flux, achieving a factor of 1.6 for regions with $t \simeq d$. This amplification persists even for relatively large sets of gap distance and thickness, up to 225 nm. This long-range enhancement of NFRHT demonstrates the system's potential to significantly expand the gap distance up to threefold compared to the two-body setup. Our findings demonstrate the potential of extended many-body systems in manipulating NFRHT, paving the way for new applications of engineered materials in thermal management technologies, and offering significant implications for the design and optimization of nanoscale thermal devices.

ACKNOWLEDGMENTS

The authors gratefully acknowledge the financial support from the National Science Foundation (NSF) through CAREER Grant No. CBET-2237003. This work was partially performed utilizing the Holland Computing Center of the University of Nebraska, which receives support from the Nebraska Research Initiative.

APPENDIX A: SOLUTION OF THE FIELD AMPLITUDES USING SCATTERING MATRIX APPROACH

1. Scattering matrix method

This section details the use of the scattering matrix method to derive the field amplitudes in a typical multilayer scenario. Let us consider a layer labeled s , with a thickness $z_{s+1} - z_s$, emitting thermal radiation. Here, it is assumed that waves with unit amplitudes are emitted in both forward (z -positive) and backward (z -negative) directions from a given source point z' located within layer s , as illustrated in Fig. 11. Since z' represents any point along the z axis within the source layer, when we calculate the radiative heat flux at a specific point z_c within layer l , it is essentially the sum of contributions from all these distributed source points within layer s . Notably, layer l could be positioned either to the left or right of the source layer s . The field within each layer results from multiple reflections within the structure and can be broken down into four principal components. Within this framework, the coefficients A and B represent the amplitudes of waves traveling forward and backward, respectively, originating from a source emitting in the forward direction. Similarly, coefficients C and D denote the amplitudes of waves traveling forward and backward, respectively, generated by a source emitting in the backward direction.

Now, to determine the coefficients A_l , B_l , C_l , and D_l , we employ the scattering matrix method (S -matrix) [111,112], which is essentially a modified version of the transfer matrix (T -matrix) approach [113] to ensure the stability of the algorithm [100]. Initially, it is important to highlight that the coefficients for forward-emitting sources (A_l and B_l) and backward-emitting sources (C_l and D_l) can be solved independently. For the purpose of this analysis, we will focus on A_l and B_l while noting that the methodology applies equivalently to C_l and D_l .

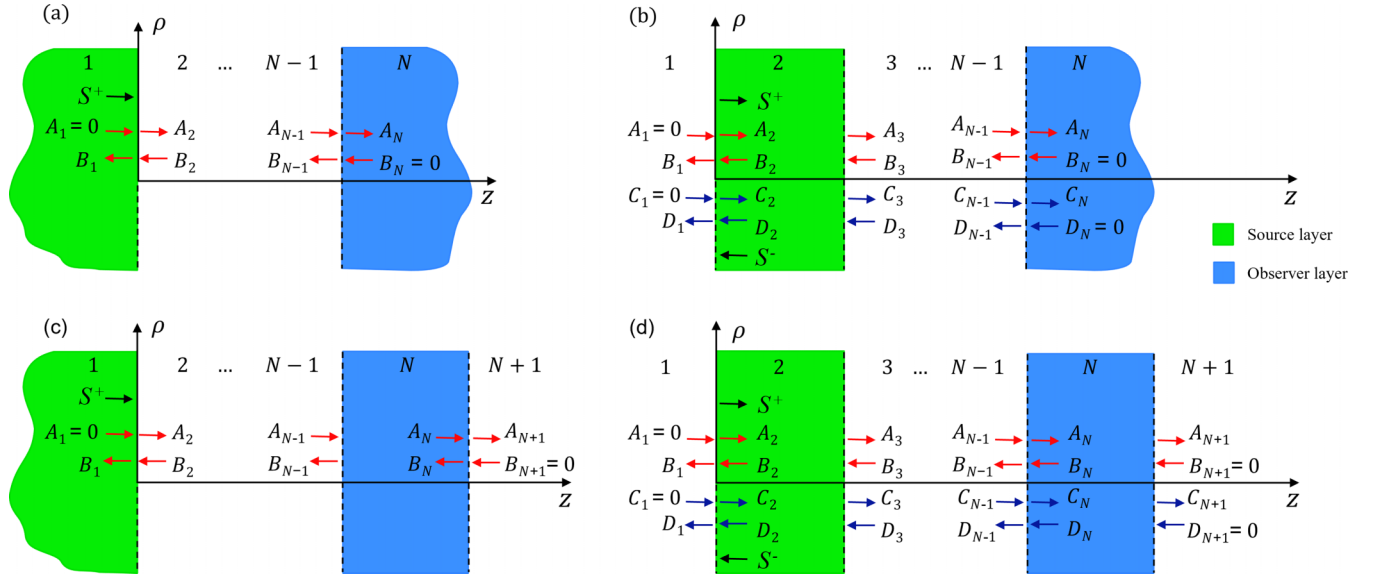


FIG. 12. Schematic of the field amplitudes for four general cases based on the thickness of the source and observer layers. (a) Both source and observer layers are half-space. (b) The source layer is a thin film and the observer layer is half-space. (c) The source layer is half-space and the observer layer is a thin film. (d) Both source and observer layers are thin films.

Therefore, the relationship between the incoming and outgoing waves across the layers 1 and l can be written as

$$\begin{bmatrix} A_l \\ B_l \end{bmatrix} = S(1, l) \begin{bmatrix} A_1 \\ B_1 \end{bmatrix}, \quad (\text{A1})$$

where $S(1, l)$ is the scattering matrix between layers 1 and l . To determine the coefficients within each layer l , the relationship between the matrix $S(1, l)$ and $S(1, l+1)$ needs to be specified. By utilizing the T -matrix relation between the coefficients A and B in layers l and $l+1$, the components of the 2×2 S -matrix at $l+1$ in terms of the S -matrix components at l are derived as

$$S_{11}(1, l+1) = \frac{S_{11}(1, l) t_{l, l+1} e^{ik_{z,l}(z_{l+1}-z_l)}}{1 - S_{12}(1, l) r_{l, l+1} e^{2ik_{z,l}(z_{l+1}-z_l)}}, \quad (\text{A2a})$$

$$S_{12}(1, l+1) = \frac{S_{12}(1, l) e^{2ik_{z,l}(z_{l+1}-z_l)} - r_{l, l+1}}{1 - S_{12}(1, l) r_{l, l+1} e^{2ik_{z,l}(z_{l+1}-z_l)}}, \quad (\text{A2b})$$

$$S_{21}(1, l+1) = \frac{S_{11}(1, l+1) S_{22}(1, l) r_{l, l+1} e^{ik_{z,l}(z_{l+1}-z_l)}}{t_{l, l+1}} + S_{21}(1, l), \quad (\text{A2c})$$

$$S_{22}(1, l+1) = \frac{S_{22}(1, l) [r_{l, l+1} S_{12}(1, l+1) + 1] e^{ik_{z,l}(z_{l+1}-z_l)}}{t_{l, l+1}}, \quad (\text{A2d})$$

with the following initialization:

$$\begin{bmatrix} S_{11}(1, 1) & S_{12}(1, 1) \\ S_{21}(1, 1) & S_{22}(1, 1) \end{bmatrix} = \begin{bmatrix} 1 & 0 \\ 0 & 1 \end{bmatrix}, \quad (\text{A3})$$

where $r_{l, l+1}$ and $t_{l, l+1}$ in Eqs. (A2a) to (A2d) represent Fresnel's reflection and transmission coefficients at the interface $l, l+1$, respectively.

It should be emphasized that the S -matrix coefficients can be computed in reference to any arbitrary layer k , not necessarily constrained to layer 1. Similarly, the initialization of the

S -matrix relative to itself $S(k, k)$ adopts a 2×2 identity matrix, with subsequent calculations of $S(k, l)$ for l ranging from $k+1$ to N carried out utilizing Eqs. (A2a) through (A2d). Notably, coefficients for each polarization state are determined independently, employing the appropriate definitions of Fresnel's transmission and reflection coefficients for TE and TM polarizations.

2. Determination of amplitude coefficients

It is critical to acknowledge that the wave emissions within the extended many-body system are assumed to originate solely from the interacting layers themselves, without any external energy source impinging on the system. Consequently, this leads to zero amplitudes for waves originating from outside the system, denoted by $A_1 = C_1 = B_N = D_N = 0$. Figure 12 provides a schematic that categorizes the field amplitudes into four general cases based on the thickness of the source and observer layers—whether they are thin films or semi-infinite slabs. To effectively determine the field amplitudes, we consider two primary scenarios: the case of a thin film emitter (with finite thickness), and the case of an emitting half-space.

a. Case of an emitting thin film

As depicted in Fig. 11, a source point z' in layer s emits waves of unit amplitude in both forward and backward directions. In this section, we focus on calculating the coefficients A_l and B_l for the source layer when emitting in the forward direction. Given that no waves enter the structure from the outside, we set $A_1 = B_N = 0$. Consequently, considering the layers 1, s , and N , we have four unknowns expressed as B_1 , A_s , B_s , and A_N , which need to be determined using the S -matrix method. This involves employing two equations: one establishing the S -matrix relation between layers 1 and s , and another equation via the S -matrix relating layers s and N .

Substituting $A_1 = 0$ in Eq. (A1), the relationship between layers 1 and s is derived as

$$A_s = S_{12}(1, s)B_s, \quad (\text{A4a})$$

$$B_1 = S_{22}(1, s)B_s. \quad (\text{A4b})$$

Similarly, considering $B_N = 0$, the relationship between layers s and N is determined as

$$\begin{bmatrix} A_N \\ B_s \end{bmatrix} = \begin{bmatrix} S_{11}(s, N) & S_{12}(s, N) \\ S_{21}(s, N) & S_{22}(s, N) \end{bmatrix} \begin{bmatrix} A_s + S^+ \\ 0 \end{bmatrix}. \quad (\text{A5})$$

It should be emphasized that when determining the coefficients of layer N , the presence of the emitting source in layer s must be taken into account, as layer N is located at a position z greater than z' . The amplitude of the source at the boundary z_s in layer s is given by $S^+ = e^{ik_z s t_s}$ where $t_s = z_{s+1} - z_s$. Equation (A5) provides the following two

$$\begin{cases} B_l = \frac{B_1}{S_{22}(1, l)} \\ A_l = S_{12}(1, l)B_l \end{cases} \quad \text{for } z < z': l = 2, \dots, s-1, \quad (\text{A8a})$$

$$\begin{cases} B_l = \frac{B_s - S_{21}(s, l)(A_s + S^+)}{S_{22}(s, l)} \\ A_l = S_{11}(s, l)(A_s + S^+) + S_{12}(s, l)B_l \end{cases} \quad \text{for } z > z': l = s+1, \dots, N-1. \quad (\text{A8b})$$

Now, let us consider the scenario where the source layer emits in the backward direction. We aim to calculate the field coefficients denoted as C_l and D_l , while already knowing that $C_1 = D_N = 0$ due to the absence of incoming waves from outside the system. Similar to the forward emitting scenario, we have four unknown coefficients (D_1 , C_s , D_s , and C_N) that can be determined using S -matrix between layers 0 and s , and layers s and N . Considering that $C_1 = 0$, the relationship between layers 1 and s can be determined using the following equation:

$$\begin{bmatrix} C_s \\ D_1 \end{bmatrix} = \begin{bmatrix} S_{11}(1, s) & S_{12}(1, s) \\ S_{21}(1, s) & S_{22}(1, s) \end{bmatrix} \begin{bmatrix} 0 \\ D_s + S^- \end{bmatrix}, \quad (\text{A9})$$

where $S^- = e^{ik_z s (-t_s)}$ is utilized to consider the influence of the source within layer s when computing the field coefficients within layer 0, located at $z < z'$.

Consequently, the relationship between layers 1 and s is derived as

$$C_s = S_{12}(1, s)(D_s + S^-), \quad (\text{A10a})$$

$$D_1 = S_{22}(1, s)(D_s + S^-). \quad (\text{A10b})$$

Following this, the S -matrix relationship between layers s and N is given by

$$\begin{bmatrix} C_N \\ D_s \end{bmatrix} = \begin{bmatrix} S_{11}(s, N) & S_{12}(s, N) \\ S_{21}(s, N) & S_{22}(s, N) \end{bmatrix} \begin{bmatrix} C_s \\ 0 \end{bmatrix}, \quad (\text{A11})$$

wherein the subsequent relationships can be obtained:

$$C_N = S_{11}(s, N)C_s, \quad (\text{A12a})$$

$$D_s = S_{21}(s, N)C_s. \quad (\text{A12b})$$

relationships:

$$A_N = S_{11}(s, N)(A_s + S^+), \quad (\text{A6a})$$

$$B_s = S_{21}(s, N)(A_s + S^+). \quad (\text{A6b})$$

Substituting Eq. (A4a) in Eq. (A6b) results in

$$B_s = \frac{S_{21}(s, N)S^+}{1 - S_{21}(s, N)S_{12}(1, s)}. \quad (\text{A7})$$

Consequently, the coefficients of layers 1, s , and N (A_s , A_N , and B_1) can be found starting from Eq. (A7). Then, utilizing the S -matrix method, a recursive scheme can determine the coefficients within each layer inside the system. Beginning with layer 1, where both A_1 and B_1 are already known, we can find A_2 and B_2 by employing the S -matrix between layers 1 and 2. Similarly, by applying the scattering matrix method between layers 1 and l when $z < z'$, and between s and l when $z > z'$, the field coefficients for any layer within the system can be derived as

$$\begin{cases} B_l = \frac{B_1}{S_{22}(1, l)} \\ A_l = S_{12}(1, l)B_l \end{cases} \quad \text{for } z < z': l = 2, \dots, s-1, \quad (\text{A8a})$$

$$\begin{cases} B_l = \frac{B_s - S_{21}(s, l)(A_s + S^+)}{S_{22}(s, l)} \\ A_l = S_{11}(s, l)(A_s + S^+) + S_{12}(s, l)B_l \end{cases} \quad \text{for } z > z': l = s+1, \dots, N-1. \quad (\text{A8b})$$

Substituting Eq. (A12b) in Eq. (A10a) yields

$$C_s = \frac{S_{12}(1, s)S^-}{1 - S_{12}(1, s)S_{21}(s, N)}, \quad (\text{A13})$$

where the coefficients of layers 1, s , and N (A_s , A_N , and D_1) can be found starting from Eq. (A13). Finally, similar to the forward emitting scenario, by applying the scattering matrix method between layers 1 and l when $z < z'$, and between s and l when $z > z'$, the field coefficients for any layer within the system can be derived as

$$\begin{cases} D_l = \frac{D_1}{S_{22}(1, l)} \\ C_l = S_{12}(1, l)D_l \end{cases} \quad \text{for } z < z': l = 2, \dots, s-1, \quad (\text{A14a})$$

$$\begin{cases} D_l = \frac{D_s - S_{21}(s, l)C_s}{S_{22}(s, l)} \\ C_l = S_{11}(s, l)C_s + S_{12}(s, l)D_l \end{cases} \quad \text{for } z > z': l = s+1, \dots, N-1. \quad (\text{A14b})$$

b. Case of an emitting half-space

In the case of an emitting half-space, all C_l and D_l coefficients for $l = 1$ to N are assumed to be zero as there is no wave emitted in the backward direction that can propagate in the one-dimensional layered medium. Similarly, if half-space N is considered a source layer, then all A_l and B_l coefficients for $l = 1$ to N should be zero. Furthermore, it can be deduced that $A_1 = B_N = 0$, as there is no field incoming from outside of the system. Then considering layers 1 and N , we are left

with two unknowns (B_1 and A_N) which can be determined by utilizing the scattering matrix method between layers 1 and N as follows:

$$\begin{bmatrix} A_N \\ B_1 \end{bmatrix} = \begin{bmatrix} S_{11}(1, N) & S_{12}(1, N) \\ S_{21}(1, N) & S_{22}(1, N) \end{bmatrix} \begin{bmatrix} S^+ \\ 0 \end{bmatrix}, \quad (\text{A15})$$

with the amplitude of the source to be $S^+ = 1$. The subsequent relationships can be inferred from Eq. (A15):

$$A_N = S_{11}(1, N), \quad (\text{A16a})$$

$$B_1 = S_{21}(1, N). \quad (\text{A16b})$$

Finally, applying the S -matrix between layers 1 and l leads to the following relationships to obtain A_l and B_l ,

$$B_l = \frac{B_1 - S_{21}(1, l)}{S_{22}(1, l)}, \quad (\text{A17a})$$

$$A_l = S_{11}(1, l) + S_{12}(1, l)B_l. \quad (\text{A17b})$$

APPENDIX B: DERIVATION OF THE EXPLICIT EXPRESSIONS FOR TRANSMISSION PROBABILITIES

In this section, we begin our discussion by introducing the Weyl representation of the magnetic and electric Dyadic Green's functions (DGFs) formalism, which have already been presented in terms of the TE- and TM-polarized unit vectors by Francoeur *et al.* [100]. Following this, the Weyl representation of the electric DGF can be expressed in tensor form as

$$\bar{\mathbf{g}}_{sl}^E(k_\rho, z_c, z', \omega) = \begin{bmatrix} g_{sl,\rho\rho}^E & 0 & g_{sl,\rho z}^E \\ 0 & g_{sl,\theta\theta}^E & 0 \\ g_{sl,z\rho}^E & 0 & g_{sl,zz}^E \end{bmatrix}, \quad (\text{B1})$$

with the electric components defined as

$$g_{sl,\rho\rho}^E(k_\rho, z_c, z', \omega) = \frac{ik_{z,l}}{2k_s k_l} \left(+A_l^{\text{TM}} e^{i[k_{z,l}(z_c-Z_l)-k_{z,s}Z']} - B_l^{\text{TM}} e^{i[-k_{z,l}(z_c-Z_l)-k_{z,s}Z']} \right. \\ \left. - C_l^{\text{TM}} e^{i[k_{z,l}(z_c-Z_l)+k_{z,s}Z']} + D_l^{\text{TM}} e^{i[-k_{z,l}(z_c-Z_l)+k_{z,s}Z']} \right), \quad (\text{B2a})$$

$$g_{sl,\rho z}^E(k_\rho, z_c, z', \omega) = \frac{ik_{z,l}k_\rho}{2k_{z,s}k_s k_l} \left(-A_l^{\text{TM}} e^{i[k_{z,l}(z_c-Z_l)-k_{z,s}Z']} + B_l^{\text{TM}} e^{i[-k_{z,l}(z_c-Z_l)-k_{z,s}Z']} \right. \\ \left. - C_l^{\text{TM}} e^{i[k_{z,l}(z_c-Z_l)+k_{z,s}Z']} + D_l^{\text{TM}} e^{i[-k_{z,l}(z_c-Z_l)+k_{z,s}Z']} \right), \quad (\text{B2b})$$

$$g_{sl,\theta\theta}^E(k_\rho, z_c, z', \omega) = \frac{i}{2k_{z,s}} \left(+A_l^{\text{TE}} e^{i[k_{z,l}(z_c-Z_l)-k_{z,s}Z']} + B_l^{\text{TE}} e^{i[-k_{z,l}(z_c-Z_l)-k_{z,s}Z']} \right. \\ \left. + C_l^{\text{TE}} e^{i[k_{z,l}(z_c-Z_l)+k_{z,s}Z']} + D_l^{\text{TE}} e^{i[-k_{z,l}(z_c-Z_l)+k_{z,s}Z']} \right), \quad (\text{B2c})$$

$$g_{sl,z\rho}^E(k_\rho, z_c, z', \omega) = \frac{ik_\rho}{2k_s k_l} \left(-A_l^{\text{TM}} e^{i[k_{z,l}(z_c-Z_l)-k_{z,s}Z']} - B_l^{\text{TM}} e^{i[-k_{z,l}(z_c-Z_l)-k_{z,s}Z']} \right. \\ \left. + C_l^{\text{TM}} e^{i[k_{z,l}(z_c-Z_l)+k_{z,s}Z']} + D_l^{\text{TM}} e^{i[-k_{z,l}(z_c-Z_l)+k_{z,s}Z']} \right), \quad (\text{B2d})$$

$$g_{sl,zz}^E(k_\rho, z_c, z', \omega) = \frac{ik_\rho^2}{2k_{z,s}k_s k_l} \left(+A_l^{\text{TM}} e^{i[k_{z,l}(z_c-Z_l)-k_{z,s}Z']} + B_l^{\text{TM}} e^{i[-k_{z,l}(z_c-Z_l)-k_{z,s}Z']} \right. \\ \left. + C_l^{\text{TM}} e^{i[k_{z,l}(z_c-Z_l)+k_{z,s}Z']} + D_l^{\text{TM}} e^{i[-k_{z,l}(z_c-Z_l)+k_{z,s}Z']} \right), \quad (\text{B2e})$$

where k_j is the magnitude of the wave vector in the layer j defined as $k_j = \sqrt{\epsilon_j} \times (\omega/c_v)$. Similarly, the Weyl representation of the magnetic DGF can be expressed in tensor form as

$$\bar{\mathbf{g}}_{sl}^H(k_\rho, z_c, z', \omega) = \begin{bmatrix} 0 & g_{sl,\rho\theta}^H & 0 \\ g_{sl,\theta\rho}^H & 0 & g_{sl,\theta z}^H \\ 0 & g_{sl,z\theta}^H & 0 \end{bmatrix}, \quad (\text{B3})$$

with the magnetic components expressed as

$$g_{sl,\rho\theta}^H(k_\rho, z_c, z', \omega) = \frac{k_{z,l}}{2k_{z,s}} \left(+A_l^{\text{TE}} e^{i[k_{z,l}(z_c-Z_l)-k_{z,s}Z']} - B_l^{\text{TE}} e^{i[-k_{z,l}(z_c-Z_l)-k_{z,s}Z']} \right. \\ \left. + C_l^{\text{TE}} e^{i[k_{z,l}(z_c-Z_l)+k_{z,s}Z']} - D_l^{\text{TE}} e^{i[-k_{z,l}(z_c-Z_l)+k_{z,s}Z']} \right), \quad (\text{B4a})$$

$$g_{sl,\theta\rho}^H(k_\rho, z_c, z', \omega) = \frac{k_l}{2k_s} \left(-A_l^{\text{TM}} e^{i[k_{z,l}(z_c-Z_l)-k_{z,s}Z']} - B_l^{\text{TM}} e^{i[-k_{z,l}(z_c-Z_l)-k_{z,s}Z']} \right. \\ \left. + C_l^{\text{TM}} e^{i[k_{z,l}(z_c-Z_l)+k_{z,s}Z']} + D_l^{\text{TM}} e^{i[-k_{z,l}(z_c-Z_l)+k_{z,s}Z']} \right), \quad (\text{B4b})$$

$$g_{sl,\theta z}^H(k_\rho, z_c, z', \omega) = \frac{k_l k_\rho}{2k_s k_{z,s}} \left(+A_l^{\text{TE}} e^{i[k_{z,l}(z_c-Z_l)-k_{z,s}Z']} + B_l^{\text{TE}} e^{i[-k_{z,l}(z_c-Z_l)-k_{z,s}Z']} \right. \\ \left. + C_l^{\text{TE}} e^{i[k_{z,l}(z_c-Z_l)+k_{z,s}Z']} + D_l^{\text{TE}} e^{i[-k_{z,l}(z_c-Z_l)+k_{z,s}Z']} \right), \quad (\text{B4c})$$

$$g_{sl,z\theta}^H(k_\rho, z_c, z', \omega) = \frac{k_\rho}{2k_{z,s}} \left(-A_l^{\text{TE}} e^{i[k_{z,l}(z_c-Z_l)-k_{z,s}Z']} - B_l^{\text{TE}} e^{i[-k_{z,l}(z_c-Z_l)-k_{z,s}Z']} \right. \\ \left. - C_l^{\text{TE}} e^{i[k_{z,l}(z_c-Z_l)+k_{z,s}Z']} - D_l^{\text{TE}} e^{i[-k_{z,l}(z_c-Z_l)+k_{z,s}Z']} \right). \quad (\text{B4d})$$

Accordingly, as previously elucidated, the spectral radiative heat flux at position $z = z_c$ within layer l along the z direction, attributed to a source layer s spanning a volume $z_{s+1} - z_s$, can be expressed as

$$\phi_{\omega, s \rightarrow l}(z_c) = \int_{k_\rho=0}^{\infty} \frac{k_\rho dk_\rho}{4\pi^2} [[\Theta_s(\omega, T_s) - \Theta_l(\omega, T_l)] \times \mathcal{T}_{s \rightarrow l}(k_\rho, \omega, z_c)]. \quad (\text{B5})$$

Now, taking into account Eq. (5), we will investigate the two scenarios outlined in Appendix A and develop explicit expressions for the transmission probabilities.

a. Case of an emitting thin film

When addressing an emitting thin film, as depicted in Fig. 11, it becomes evident that integrating over Z' is necessary to consider all arbitrary point sources potentially located within layer s . To this end, we first separate the nonzero Weyl

components of the DGF between layers s and l at location z_c in terms of TE- and TM-polarization for convenience, and then perform analytical integration to eliminate the z' dependency. Here, upon examining Eq. (7), the expression $g_{sl,\rho\rho}^E g_{sl,\theta\rho}^{H*} + g_{sl,\rho z}^E g_{sl,\theta z}^{H*}$ can be interpreted as a term related to the transmission probability of TM-polarized waves, whereas $g_{sl,\theta\theta}^E g_{sl,\theta\theta}^{H*}$ pertains to TE-polarized waves. Subsequently, integrating the product of the mentioned Weyl components of the DGF over the volume of the emitter at $z_c = z_l$ yields the following expressions for TM- and TE-polarization, respectively:

$$\begin{aligned} & g_{sl,\rho\rho}^E g_{sl,\theta\rho}^{H*}(k_\rho, z_c = z_l, \omega) + g_{sl,\rho z}^E g_{sl,\theta z}^{H*}(k_\rho, z_c = z_l, \omega) \\ &= \frac{ik_{z,l} k_l^*}{8k'_{z,s} k''_{z,s} k_l |k_s|^2 |k_{z,s}|^2} \left[\begin{aligned} & k'_{z,s} (e^{2k'_{z,s} t_s} - 1) (|k_{z,s}|^2 + k_\rho^2) (-|A_l^{\text{TM}}|^2 - A_l^{\text{TM}} B_l^{\text{TM}*} + A_l^{\text{TM}*} B_l^{\text{TM}} + |B_l^{\text{TM}}|^2) \\ & + ik''_{z,s} (e^{-2ik''_{z,s} t_s} - 1) (|k_{z,s}|^2 - k_\rho^2) (A_l^{\text{TM}} C_l^{\text{TM}*} + A_l^{\text{TM}} D_l^{\text{TM}*} - B_l^{\text{TM}} C_l^{\text{TM}*} - B_l^{\text{TM}} D_l^{\text{TM}*}) \\ & + ik''_{z,s} (1 - e^{2ik''_{z,s} t_s}) (|k_{z,s}|^2 - k_\rho^2) (A_l^{\text{TM}*} C_l^{\text{TM}} + B_l^{\text{TM}*} C_l^{\text{TM}} - A_l^{\text{TM}*} D_l^{\text{TM}} - B_l^{\text{TM}*} D_l^{\text{TM}}) \\ & + k'_{z,s} (1 - e^{-2k'_{z,s} t_s}) (|k_{z,s}|^2 + k_\rho^2) (-|C_l^{\text{TM}}|^2 - C_l^{\text{TM}} D_l^{\text{TM}*} + C_l^{\text{TM}*} D_l^{\text{TM}} + |D_l^{\text{TM}}|^2) \end{aligned} \right], \quad (\text{B6a}) \end{aligned}$$

$$\begin{aligned} & g_{sl,\theta\theta}^E g_{sl,\rho\theta}^{H*}(k_\rho, z_c = z_l, \omega) \\ &= \frac{ik_{z,l}^*}{8k'_{z,s} k''_{z,s} |k_{z,s}|^2} \left[\begin{aligned} & k'_{z,s} (e^{2k'_{z,s} t_s} - 1) (|A_l^{\text{TE}}|^2 - A_l^{\text{TE}} B_l^{\text{TE}*} + A_l^{\text{TE}*} B_l^{\text{TE}} - |B_l^{\text{TE}}|^2) \\ & + ik''_{z,s} (e^{-2ik''_{z,s} t_s} - 1) (A_l^{\text{TE}} C_l^{\text{TE}*} - A_l^{\text{TE}} D_l^{\text{TE}*} + B_l^{\text{TE}} C_l^{\text{TE}*} - B_l^{\text{TE}} D_l^{\text{TE}*}) \\ & + ik''_{z,s} (1 - e^{2ik''_{z,s} t_s}) (A_l^{\text{TE}*} C_l^{\text{TE}} - B_l^{\text{TE}*} C_l^{\text{TE}} + A_l^{\text{TE}*} D_l^{\text{TE}} - B_l^{\text{TE}*} D_l^{\text{TE}}) \\ & + k'_{z,s} (1 - e^{-2k'_{z,s} t_s}) (|C_l^{\text{TE}}|^2 - C_l^{\text{TE}} D_l^{\text{TE}*} + C_l^{\text{TE}*} D_l^{\text{TE}} - |D_l^{\text{TE}}|^2) \end{aligned} \right]. \quad (\text{B6b}) \end{aligned}$$

In this context, it is crucial to acknowledge that when $z_c = z_l$, the thickness of the observer layer up to this point (z_c) becomes insignificant ($t_c = 0$). As a result, the related exponential terms simplify to $e^{2k''_{z,s} t_c} = 1$. Consequently, by integrating the Weyl DGF components over z' at $z_c = z_l$ and substituting them into Eq. (5), the specific expression for the transmission probability of an emitting thin film can be obtained.

b. Case of an emitting half-space

In the scenario of a semi-infinite source configuration, the dependency on z' of the Weyl DGF components can be explicitly isolated as expressed in Eq. (6). Then, performing analytical integration over z' from $z_j = -\infty$ to $z_{j+1} = 0$ eliminates the dependence of DGFs on z' :

$$\begin{aligned} & \int_{-\infty}^0 g_{sl,\alpha\beta}^E(k_\rho, z_c, z', \omega) g_{sl,\alpha\beta}^{H*}(k_\rho, z_c, z', \omega) dz' \\ &= \int_{-\infty}^0 g_{sl,\alpha\beta}^E(k_\rho, z_c, \omega) g_{sl,\alpha\beta}^{H*}(k_\rho, z_c, \omega) e^{2k''_{z,s} z'} dz' \\ &= \frac{g_{sl,\alpha\beta}^E(k_\rho, z_c, \omega) g_{sl,\alpha\beta}^{H*}(k_\rho, z_c, \omega)}{2k''_{z,s}}. \quad (\text{B7}) \end{aligned}$$

Accordingly, in this scenario, the electric Weyl DGF components required for calculating the spectral heat flux incident on the observer layer are given by setting $z_c = z_l$:

$$g_{sl,\rho\rho}^E(k_\rho, z_c = z_l, \omega) = \frac{ik_{z,l}}{2k_s k_l} \begin{pmatrix} +A_l^{\text{TM}} - B_l^{\text{TM}} \\ -C_l^{\text{TM}} + D_l^{\text{TM}} \end{pmatrix}, \quad (\text{B8a})$$

$$g_{sl,\rho z}^E(k_\rho, z_c = z_l, \omega) = \frac{ik_{z,l} k_\rho}{2k_{z,s} k_s k_l} \begin{pmatrix} -A_l^{\text{TM}} + B_l^{\text{TM}} \\ -C_l^{\text{TM}} + D_l^{\text{TM}} \end{pmatrix}, \quad (\text{B8b})$$

$$g_{sl,\theta\theta}^E(k_\rho, z_c = z_l, \omega) = \frac{i}{2k_{z,s}} \begin{pmatrix} +A_l^{\text{TE}} + B_l^{\text{TE}} \\ +C_l^{\text{TE}} + D_l^{\text{TE}} \end{pmatrix}, \quad (\text{B8c})$$

$$g_{sl,z\rho}^E(k_\rho, z_c = z_l, \omega) = \frac{ik_\rho}{2k_s k_l} \begin{pmatrix} -A_l^{\text{TM}} - B_l^{\text{TM}} \\ +C_l^{\text{TM}} + D_l^{\text{TM}} \end{pmatrix}, \quad (\text{B8d})$$

$$g_{sl,zz}^E(k_\rho, z_c = z_l, \omega) = \frac{ik_\rho^2}{2k_{z,s} k_s k_l} \begin{pmatrix} +A_l^{\text{TM}} + B_l^{\text{TM}} \\ +C_l^{\text{TM}} + D_l^{\text{TM}} \end{pmatrix}. \quad (\text{B8e})$$

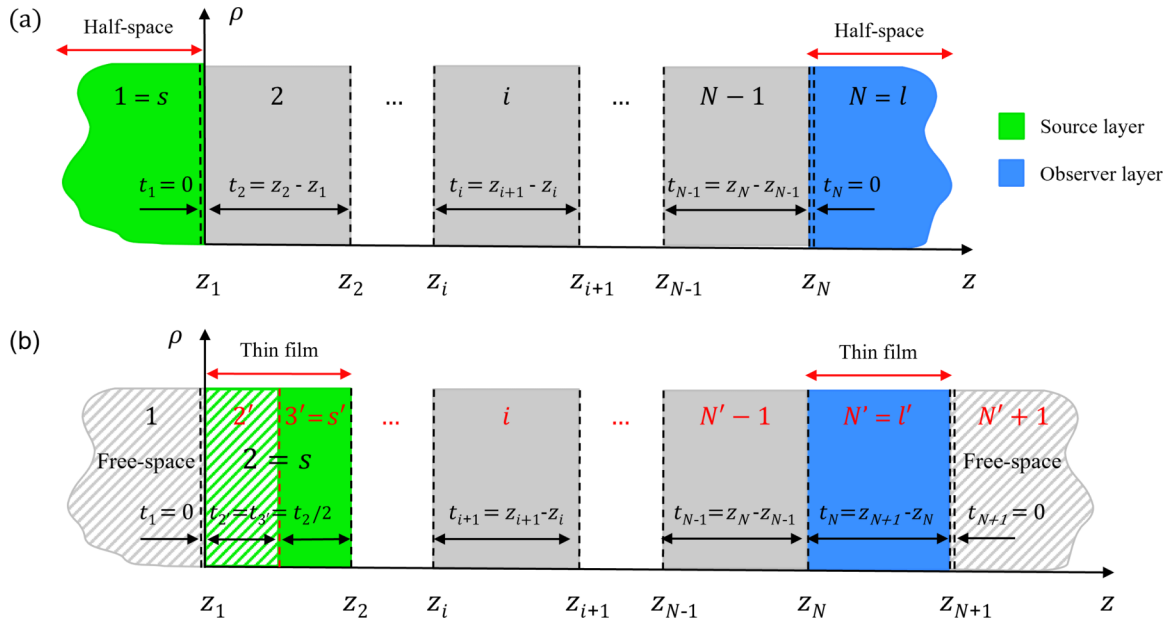


FIG. 13. Schematic of two common scenarios of NFRHT within a one-dimensional layered system: (a) Configuration featuring the source and observer layers as half-spaces. (b) Configuration incorporating thin films for both the source and observer layers.

Similarly, the magnetic Weyl DGF components at $z_c = z_l$ are provided as

$$g_{sl,\rho\theta}^H(k_\rho, z_c = z_l, \omega) = \frac{k_{z,l}}{2k_{z,s}} \begin{pmatrix} +A_l^{\text{TE}} - B_l^{\text{TE}} \\ +C_l^{\text{TE}} - D_l^{\text{TE}} \end{pmatrix}, \quad (\text{B9a})$$

$$g_{sl,\theta\rho}^E(k_\rho, z_c = z_l, \omega) = \frac{k_l}{2k_s} \begin{pmatrix} -A_l^{\text{TM}} - B_l^{\text{TM}} \\ +C_l^{\text{TM}} + D_l^{\text{TM}} \end{pmatrix}, \quad (\text{B9b})$$

$$g_{sl,\theta z}^E(k_\rho, z_c = z_l, \omega) = \frac{k_l k_\rho}{2k_s k_{z,s}} \begin{pmatrix} +A_l^{\text{TM}} + B_l^{\text{TM}} \\ +C_l^{\text{TM}} + D_l^{\text{TM}} \end{pmatrix}, \quad (\text{B9c})$$

$$g_{sl,z\theta}^E(k_\rho, z_c = z_l, \omega) = \frac{k_\rho}{2k_{z,s}} \begin{pmatrix} -A_l^{\text{TE}} - B_l^{\text{TE}} \\ -C_l^{\text{TE}} - D_l^{\text{TE}} \end{pmatrix}. \quad (\text{B9d})$$

Finally, substituting the derived Weyl DGF components at $z_c = z_l$ into Eq. (7) results in the explicit form of the transmission probability for an emitting half-space.

With explicit expressions for transmission probabilities derived, we now focus on computing NFRHT in two specific scenarios where we consider both the source and the observer to be (1) semi-infinite slabs or (2) thin film layers, as depicted in Fig. 13. When dealing with a semi-infinite slab for either the source or observer layer, as shown in Fig. 13(a), we assign a thickness of $t = 0$ for that particular layer. The thickness for subsequent layers is defined by $t_i = z_{i+1} - z_i$. Conversely, when the configuration involves thin film layers for both the source and observer, as shown in Fig. 13(b),

it becomes necessary to introduce hypothetical semi-infinite vacuum slabs at both ends of the system. These slabs are assigned a thickness of $t = 0$ and a dielectric constant of $\epsilon = 1$, positioned before the thin source layer and after the observer layer, respectively, increasing the total number of interacting layers in the S -matrix method by two. Additionally, when dealing with thin-film emitters, to prevent numerical instabilities, we divide the thin-film emitter with a thickness of t_s into two equally thinner sublayers [100], each with a thickness of $t_{s1} = t_{s2} = t_s/2$. As a result, our original N layered system is transformed into a $N + 1$ layered system. Following this, we deliberately designate the latter sublayer [depicted by the green section in Fig. 13(b)] with a thickness of t_{s2} as the adjusted source layer to ensure the numerical stability of the S -matrix algorithm. Then, we calculate the field amplitudes using the S -matrix method, incorporating the index of the newly adjusted source layer (second sublayer) indicated by $s' = s + 1$. Similarly, the observer layer is now represented by $l' = l + 1$ due to the splitting of the emitter layer. The system is thus effectively considered as having $N + 1$ layers. It is important to ensure that the integration over z' covers the entire thickness of the source layer. Therefore, following the computation of the field amplitudes, during the integration of the Weyl DGF components over z' , we treat both sublayers [dashed and green sections in Fig. 13(b)] as a unified source layer with a thickness of $t_s = 2t_{s2}$. Further insights into the algorithm required to tackle the NFRHT problem using this S -matrix approach can be found in Ref. [100].

[1] C.-L. Tien and G. Chen, Challenges in microscale conductive and radiative heat transfer, *J. Heat Transfer*. **116**, 799 (1994).

[2] K. Joulain, J.-P. Mulet, F. Marquier, R. Carminati, and J.-J. Greffet, Surface electromagnetic waves thermally excited: Ra-

- diative heat transfer, coherence properties and Casimir forces revisited in the near field, *Surf. Sci. Rep.* **57**, 59 (2005).
- [3] J.-P. Mulet, K. Joulain, R. Carminati, and J.-J. Greffet, Enhanced radiative heat transfer at nanometric distances, *Microscale Thermophys. Eng.* **6**, 209 (2002).
- [4] L. Hu, A. Narayanaswamy, X. Chen, and G. Chen, Near-field thermal radiation between two closely spaced glass plates exceeding Planck's blackbody radiation law, *Appl. Phys. Lett.* **92**, 133106 (2008).
- [5] M. Francoeur and M. P. Mengüç, Role of fluctuational electrodynamics in near-field radiative heat transfer, *J. Quantum Spectrosc. Radiat. Transf.* **109**, 280 (2008).
- [6] B. Song, D. Thompson, A. Fiorino, Y. Ganjeh, P. Reddy, and E. Meyhofer, Radiative heat conductances between dielectric and metallic parallel plates with nanoscale gaps, *Nat. Nanotechnol.* **11**, 509 (2016).
- [7] Y. De Wilde, F. Formanek, R. Carminati, B. Gralak, P.-A. Lemoine, K. Joulain, J.-P. Mulet, Y. Chen, and J.-J. Greffet, Thermal radiation scanning tunnelling microscopy, *Nature (London)* **444**, 740 (2006).
- [8] A. Kittel, U. F. Wischnath, J. Welker, O. Huth, F. Rueting, and S.-A. Biehs, Near-field thermal imaging of nanostructured surfaces, *Appl. Phys. Lett.* **93**, 193109 (2008).
- [9] Y. Zhang, W. Zhu, F. Hui, M. Lanza, T. Borca-Tasciuc, and M. Muñoz Rojo, A review on principles and applications of scanning thermal microscopy, *Adv. Funct. Mater.* **30**, 1900892 (2020).
- [10] M. H. Kryder, E. C. Gage, T. W. McDaniel, W. A. Challener, R. E. Rottmayer, G. Ju, Y.-T. Hsia, and M. F. Erden, Heat assisted magnetic recording, *Proc. IEEE* **96**, 1810 (2008).
- [11] W. Challener, C. Peng, A. Itagi, D. Karns, W. Peng, Y. Peng, X. Yang, X. Zhu, N. Gokemeijer, Y.-T. Hsia *et al.*, Heat-assisted magnetic recording by a near-field transducer with efficient optical energy transfer, *Nat. Photon.* **3**, 220 (2009).
- [12] D. Conteduca, I. Barth, G. Pitruzzello, C. P. Reardon, E. R. Martins, and T. F. Krauss, Dielectric nanohole array metasurface for high-resolution near-field sensing and imaging, *Nat. Commun.* **12**, 3293 (2021).
- [13] G. T. Papadakis, M. Orenstein, E. Yablonovitch, and S. Fan, Thermodynamics of light management in near-field thermophotovoltaics, *Phys. Rev. Appl.* **16**, 064063 (2021).
- [14] R. Mittapally, B. Lee, L. Zhu, A. Reihani, J. W. Lim, D. Fan, S. R. Forrest, P. Reddy, and E. Meyhofer, Near-field thermophotovoltaics for efficient heat to electricity conversion at high power density, *Nat. Commun.* **12**, 4364 (2021).
- [15] M. Ghashami, S. K. Cho, and K. Park, Near-field enhanced thermionic energy conversion for renewable energy recycling, *J. Quantum Spectrosc. Radiat. Transf.* **198**, 59 (2017).
- [16] B. Wang, C. Lin, K. H. Teo, and Z. Zhang, Thermoradiative device enhanced by near-field coupled structures, *J. Quantum Spectrosc. Radiat. Transf.* **196**, 10 (2017).
- [17] E. Tervo, E. Bagherisereshki, and Z. Zhang, Near-field radiative thermoelectric energy converters: a review, *Front. Energy* **12**, 5 (2018).
- [18] B. Guha, C. Otey, C. B. Poitras, S. Fan, and M. Lipson, Near-field radiative cooling of nanostructures, *Nano Lett.* **12**, 4546 (2012).
- [19] M. Lim, J. Song, S. S. Lee, and B. J. Lee, Tailoring near-field thermal radiation between metallo-dielectric multilayers using coupled surface plasmon polaritons, *Nat. Commun.* **9**, 4302 (2018).
- [20] L. Ge, Z. Xu, Y. Cang, and K. Gong, Modulation of near-field radiative heat transfer between graphene sheets by strain engineering, *Opt. Express* **27**, A1109 (2019).
- [21] I. Latella, S.-A. Biehs, and P. Ben-Abdallah, Smart thermal management with near-field thermal radiation, *Opt. Express* **29**, 24816 (2021).
- [22] M.-Q. Yuan, Y. Zhang, S.-H. Yang, and H.-L. Yi, Active control of the near-field radiative heat transfer between two metal plates through the external electric field, *Int. J. Therm. Sci.* **171**, 107208 (2022).
- [23] B. Song, Y. Ganjeh, S. Sadat, D. Thompson, A. Fiorino, V. Fernández-Hurtado, J. Feist, F. J. Garcia-Vidal, J. C. Cuevas, P. Reddy *et al.*, Enhancement of near-field radiative heat transfer using polar dielectric thin films, *Nat. Nanotechnol.* **10**, 253 (2015).
- [24] R. St-Gelais, L. Zhu, S. Fan, and M. Lipson, Near-field radiative heat transfer between parallel structures in the deep subwavelength regime, *Nat. Nanotechnol.* **11**, 515 (2016).
- [25] A. Fiorino, D. Thompson, L. Zhu, B. Song, P. Reddy, and E. Meyhofer, Giant enhancement in radiative heat transfer in sub-30 nm gaps of plane parallel surfaces, *Nano Lett.* **18**, 3711 (2018).
- [26] V. Musilová, T. Králík, T. Fořt, and M. Macek, Strong suppression of near-field radiative heat transfer by superconductivity in NbN, *Phys. Rev. B* **99**, 024511 (2019).
- [27] C.-L. Zhou, Y. Zharig, H.-L. Yi, and L. Qu, Radiation-based near-field thermal rectification via asymmetric nanostructures of the single material, in *Proceedings of the Photonics and Electromagnetics Research Symposium-Spring (PIERS-Spring)* (IEEE, Piscataway, NJ, 2019), pp. 2652–2658.
- [28] M. Francoeur, R. Vaillon, and M. P. Mengüç, Thermal impacts on the performance of nanoscale-gap thermophotovoltaic power generators, *IEEE Trans. Energy Conv.* **26**, 686 (2011).
- [29] R. Messina and P. Ben-Abdallah, Graphene-based photovoltaic cells for near-field thermal energy conversion, *Sci. Rep.* **3**, 1383 (2013).
- [30] B. Zhao, L. Wang, Y. Shuai, and Z. M. Zhang, Thermophotovoltaic emitters based on a two-dimensional grating/thin-film nanostructure, *Int. J. Heat Mass Transf.* **67**, 637 (2013).
- [31] A. Lenert, D. M. Bierman, Y. Nam, W. R. Chan, I. Celanović, M. Soljačić, and E. N. Wang, A nanophotonic solar thermophotovoltaic device, *Nat. Nanotechnol.* **9**, 126 (2014).
- [32] V. B. Svetovoy and G. Palasantzas, Graphene-on-silicon near-field thermophotovoltaic cell, *Phys. Rev. Appl.* **2**, 034006 (2014).
- [33] A. Fiorino, L. Zhu, D. Thompson, R. Mittapally, P. Reddy, and E. Meyhofer, Nanogap near-field thermophotovoltaics, *Nat. Nanotechnol.* **13**, 806 (2018).
- [34] R. Mittapally, A. Majumder, P. Reddy, and E. Meyhofer, Near-field thermophotovoltaic energy conversion: Progress and opportunities, *Phys. Rev. Appl.* **19**, 037002 (2023).
- [35] S. Basu and M. Francoeur, Near-field radiative transfer based thermal rectification using doped silicon, *Appl. Phys. Lett.* **98**, 113106 (2011).
- [36] Y. Yang, S. Basu, and L. Wang, Radiation-based near-field thermal rectification with phase transition materials, *Appl. Phys. Lett.* **103**, 163101 (2013).

- [37] L. Wang and Z. Zhang, Thermal rectification enabled by near-field radiative heat transfer between intrinsic silicon and a dissimilar material, *Nanos. Microscale Thermophys. Eng.* **17**, 337 (2013).
- [38] Z. Zheng, X. Liu, A. Wang, and Y. Xuan, Graphene-assisted near-field radiative thermal rectifier based on phase transition of vanadium dioxide (VO₂), *Int. J. Heat Mass Transf.* **109**, 63 (2017).
- [39] G. Xu, J. Sun, H. Mao, and T. Pan, Highly efficient near-field thermal rectification between insb and graphene-coated SiO₂, *J. Quantum Spectrosc. Radiat. Transf.* **220**, 140 (2018).
- [40] C.-H. Wang, H. Bian, C.-C. Pan, and Z.-Y. Jiang, Near-field thermal rectification via an InSb/graphene/3C-SiC-nanowire heterostructure, *Int. J. Therm. Sci.* **194**, 108581 (2023).
- [41] R. Yang, A. Narayanaswamy, and G. Chen, Surface-plasmon coupled nonequilibrium thermoelectric refrigerators and power generators, *J. Comput. Theoret. Nanosci.* **2**, 75 (2005).
- [42] C. Lin, B. Wang, K. H. Teo, and Z. Zhang, A coherent description of thermal radiative devices and its application on the near-field negative electroluminescent cooling, *Energy* **147**, 177 (2018).
- [43] L. Zhu, A. Fiorino, D. Thompson, R. Mittapally, E. Meyhofer, and P. Reddy, Near-field photonic cooling through control of the chemical potential of photons, *Nature (London)* **566**, 239 (2019).
- [44] R. Messina, J.-P. Hugonin, J.-J. Greffet, F. Marquier, Y. De Wilde, A. Belarouci, L. Frechette, Y. Cordier, and P. Ben-Abdallah, Tuning the electromagnetic local density of states in graphene-covered systems via strong coupling with graphene plasmons, *Phys. Rev. B* **87**, 085421 (2013).
- [45] X. Liu and Z. Zhang, Graphene-assisted near-field radiative heat transfer between corrugated polar materials, *Appl. Phys. Lett.* **104**, 251911 (2014).
- [46] A. Wang, Z. Zheng, and Y. Xuan, Near-field radiative thermal control with graphene covered on different materials, *J. Quantum Spectrosc. Radiat. Transf.* **180**, 117 (2016).
- [47] R. Messina, P. Ben-Abdallah, B. Guizal, and M. Antezza, Graphene-based amplification and tuning of near-field radiative heat transfer between dissimilar polar materials, *Phys. Rev. B* **96**, 045402 (2017).
- [48] S. Zare, B. Zeinali Tajani, and S. Edalatpour, Effect of nonlocal electrical conductivity on near-field radiative heat transfer between graphene sheets, *Phys. Rev. B* **105**, 125416 (2022).
- [49] S.-A. Biehs, M. Tschikin, and P. Ben-Abdallah, Hyperbolic metamaterials as an analog of a blackbody in the near field, *Phys. Rev. Lett.* **109**, 104301 (2012).
- [50] B. Zhao and Z. Zhang, Enhanced photon tunneling by surface plasmon-phonon polaritons in graphene/HbN heterostructures, *J. Heat Transfer* **139**, 022701 (2017).
- [51] X. Wu, C. Fu, and Z. Zhang, Influence of hbn orientation on the near-field radiative heat transfer between graphene/HbN heterostructures, *J. Photon. Energy* **9**, 032702 (2019).
- [52] X. Wu and C. Fu, Near-field radiative heat transfer between uniaxial hyperbolic media: Role of volume and surface phonon polaritons, *J. Quantum Spectrosc. Radiat. Transf.* **258**, 107337 (2021).
- [53] R. Liu, C. Zhou, Y. Zhang, Z. Cui, X. Wu, and H. Yi, Near-field radiative heat transfer in hyperbolic materials, *Int. J. Extreme Manufact.* **4**, 032002 (2022).
- [54] S.-A. Biehs, F. S. Rosa, and P. Ben-Abdallah, Modulation of near-field heat transfer between two gratings, *Appl. Phys. Lett.* **98**, 243102 (2011).
- [55] X. Liu, J. Shen, and Y. Xuan, Pattern-free thermal modulator via thermal radiation between van der Waals materials, *J. Quantum Spectrosc. Radiat. Transf.* **200**, 100 (2017).
- [56] X. Liu, R. Zhang, and Z. Zhang, Near-field radiative heat transfer with doped-silicon nanostructured metamaterials, *Int. J. Heat Mass Transf.* **73**, 389 (2014).
- [57] S. V. Boriskina, J. K. Tong, Y. Huang, J. Zhou, V. Chiloyan, and G. Chen, Enhancement and tunability of near-field radiative heat transfer mediated by surface plasmon polaritons in thin plasmonic films, in *Photonics* (MDPI, Basel, Switzerland, 2015), Vol. 2, pp. 659–683.
- [58] H. Iizuka and S. Fan, Significant enhancement of near-field electromagnetic heat transfer in a multilayer structure through multiple surface-states coupling, *Phys. Rev. Lett.* **120**, 063901 (2018).
- [59] S. Basu and L. Wang, Near-field radiative heat transfer between doped silicon nanowire arrays, *Appl. Phys. Lett.* **102**, 053101 (2013).
- [60] J.-Y. Chang, S. Basu, and L. Wang, Indium tin oxide nanowires as hyperbolic metamaterials for near-field radiative heat transfer, *J. Appl. Phys.* **117**, 054309 (2015).
- [61] S.-A. Biehs, P. Ben-Abdallah, F. S. Rosa, K. Joulain, and J.-J. Greffet, Nanoscale heat flux between nanoporous materials, *Opt. Express* **19**, A1088 (2011).
- [62] J. Lussange, R. Guérout, F. S. S. Rosa, J.-J. Greffet, A. Lambrecht, and S. Reynaud, Radiative heat transfer between two dielectric nanogratings in the scattering approach, *Phys. Rev. B* **86**, 085432 (2012).
- [63] X. Liu, B. Zhao, and Z. M. Zhang, Enhanced near-field thermal radiation and reduced Casimir stiction between doped-Si gratings, *Phys. Rev. A* **91**, 062510 (2015).
- [64] X. Liu and Z. Zhang, Near-field thermal radiation between metasurfaces, *ACS Photon.* **2**, 1320 (2015).
- [65] Y. Yang and L. Wang, Spectrally enhancing near-field radiative transfer between metallic gratings by exciting magnetic polaritons in nanometric vacuum gaps, *Phys. Rev. Lett.* **117**, 044301 (2016).
- [66] R. Messina, A. Noto, B. Guizal, and M. Antezza, Radiative heat transfer between metallic gratings using fourier modal method with adaptive spatial resolution, *Phys. Rev. B* **95**, 125404 (2017).
- [67] P. Ben-Abdallah and K. Joulain, Fundamental limits for noncontact transfers between two bodies, *Phys. Rev. B* **82**, 121419(R) (2010).
- [68] S.-A. Biehs, E. Rousseau, and J.-J. Greffet, Mesoscopic description of radiative heat transfer at the nanoscale, *Phys. Rev. Lett.* **105**, 234301 (2010).
- [69] P. Ben-Abdallah, S.-A. Biehs, and K. Joulain, Many-body radiative heat transfer theory, *Phys. Rev. Lett.* **107**, 114301 (2011).
- [70] R. Messina, M. Tschikin, S.-A. Biehs, and P. Ben-Abdallah, Fluctuation-electrodynamics theory and dynamics of heat transfer in systems of multiple dipoles, *Phys. Rev. B* **88**, 104307 (2013).
- [71] K. Säskilähti, J. Oksanen, and J. Tulkki, Quantum Langevin equation approach to electromagnetic energy transfer between

- dielectric bodies in an inhomogeneous environment, *Phys. Rev. B* **89**, 134301 (2014).
- [72] M. Nikbakht, Radiative heat transfer in anisotropic many-body systems: Tuning and enhancement, *J. Appl. Phys.* **116**, 094307 (2014).
- [73] R. Messina and M. Antezza, Three-body radiative heat transfer and Casimir-Lifshitz force out of thermal equilibrium for arbitrary bodies, *Phys. Rev. A* **89**, 052104 (2014).
- [74] B. Müller, R. Incardone, M. Antezza, T. Emig, and M. Krüger, Many-body heat radiation and heat transfer in the presence of a nonabsorbing background medium, *Phys. Rev. B* **95**, 085413 (2017).
- [75] K. Asheichyk, B. Müller, and M. Krüger, Heat radiation and transfer for point particles in arbitrary geometries, *Phys. Rev. B* **96**, 155402 (2017).
- [76] M. Krüger, G. Bimonte, T. Emig, and M. Kardar, Trace formulas for nonequilibrium Casimir interactions, heat radiation, and heat transfer for arbitrary objects, *Phys. Rev. B* **86**, 115423 (2012).
- [77] L. Zhu, Y. Guo, and S. Fan, Theory of many-body radiative heat transfer without the constraint of reciprocity, *Phys. Rev. B* **97**, 094302 (2018).
- [78] L. P. Walter, E. J. Tervo, and M. Francoeur, Near-field radiative heat transfer between irregularly shaped dielectric particles modeled with the discrete system Green's function method, *Phys. Rev. B* **106**, 195417 (2022).
- [79] J.-Y. Wang, Y. Zhang, C.-L. Zhou, Y. Shuai, and H.-L. Yi, Enhanced radiative heat transfer via propagating surface modes in a dielectric nanowire, *Phys. Rev. B* **109**, 075423 (2024).
- [80] K. Asheichyk and M. Krüger, Heat radiation and transfer for nanoparticles in the presence of a cylinder, *Phys. Rev. B* **109**, 125412 (2024).
- [81] R. Messina, M. Antezza, and P. Ben-Abdallah, Three-body amplification of photon heat tunneling, *Phys. Rev. Lett.* **109**, 244302 (2012).
- [82] Z. Zheng and Y. Xuan, Enhancement or suppression of the near-field radiative heat transfer between two materials, *Nanoscale Microscale Thermophys. Eng.* **15**, 237 (2011).
- [83] H. Simchi, Graphene-based three-body amplification of photon heat tunneling, *J. Appl. Phys.* **121**, 094301 (2017).
- [84] R. Messina, P. Ben-Abdallah, B. Guizal, M. Antezza, and S.-A. Biehs, Hyperbolic waveguide for long-distance transport of near-field heat flux, *Phys. Rev. B* **94**, 104301 (2016).
- [85] P. Ben-Abdallah and S.-A. Biehs, Near-field thermal transistor, *Phys. Rev. Lett.* **112**, 044301 (2014).
- [86] W. Gu, G.-H. Tang, and W.-Q. Tao, Thermal switch and thermal rectification enabled by near-field radiative heat transfer between three slabs, *Int. J. Heat Mass Transf.* **82**, 429 (2015).
- [87] D. Thompson, L. Zhu, E. Meyhofer, and P. Reddy, Nanoscale radiative thermal switching via multi-body effects, *Nat. Nanotechnol.* **15**, 99 (2020).
- [88] P. Ben-Abdallah and S.-A. Biehs, Towards Boolean operations with thermal photons, *Phys. Rev. B* **94**, 241401(R) (2016).
- [89] C. Kathmann, M. Reina, R. Messina, P. Ben-Abdallah, and S.-A. Biehs, Scalable radiative thermal logic gates based on nanoparticle networks, *Sci. Rep.* **10**, 3596 (2020).
- [90] V. Kubyt'skiy, S.-A. Biehs, and P. Ben-Abdallah, Radiative bistability and thermal memory, *Phys. Rev. Lett.* **113**, 074301 (2014).
- [91] H. Prod'homme, J. Ordonez-Miranda, Y. Ezzahri, J. Drévilion, and K. Joulain, VO₂-based radiative thermal transistor with a semi-transparent base, *J. Quantum Spectrosc. Radiat. Transf.* **210**, 52 (2018).
- [92] B. Wang, J. Zhang, and C. Li, An intermediate modulator enhanced the near-field thermal radiation of semiconductor vanadium dioxide, *Results Phys.* **33**, 105199 (2022).
- [93] M.-J. He, X. Guo, H. Qi, Z.-H. Zheng, M. Antezza, and H.-P. Tan, Performance improvement of three-body radiative diodes driven by graphene surface plasmon polaritons, *Phys. Chem. Chem. Phys.* **25**, 20782 (2023).
- [94] L. Qu, E. Moncada-Villa, J.-L. Fang, Y. Zhang, and H.-L. Yi, Tunable magnetic field effects on the near-field radiative heat transfer in planar three-body systems, *Phys. Rev. B* **107**, 205405 (2023).
- [95] S. Fu, T. Wang, T. Yu, and Q. Liao, Near-field radiative heat transfer in three-body system based on topological insulator Bi₂Se₃, *AIP Adv.* **13**, 075121 (2023).
- [96] Y. H. Kan, C. Y. Zhao, and Z. M. Zhang, Near-field radiative heat transfer in three-body systems with periodic structures, *Phys. Rev. B* **99**, 035433 (2019).
- [97] Y. Kan and C. Zhao, Near field radiative heat transfer in asymmetric three-grating systems, *Int. J. Heat Mass Transf.* **171**, 121124 (2021).
- [98] F. Chen, G. An, and Z. Xu, Performance analysis of three-body near-field thermophotovoltaic systems with an intermediate modulator, *J. Quantum Spectrosc. Radiat. Transf.* **258**, 107395 (2021).
- [99] X. Li, T. Wang, T. Yu, and Q. Liao, Near-field radiative heat transfer in the three-body system made of nanoporous silicon carbide, *Eur. Phys. J. B* **95**, 140 (2022).
- [100] M. Francoeur, M. P. Mengüç, and R. Vaillon, Solution of near-field thermal radiation in one-dimensional layered media using dyadic Green's functions and the scattering matrix method, *J. Quantum Spectrosc. Radiat. Transf.* **110**, 2002 (2009).
- [101] E. D. Palik, *Handbook of Optical Constants of Solids* (Academic Press, San Diego, CA, 1998), Vol. 3.
- [102] B. Yang and Q. Dai, Highly-efficient radiative thermal rectifiers based on near-field gap variations, *Nanoscale* **14**, 16978 (2022).
- [103] P. Tian, S. Li, L. Gao, and Y. Xu, Ultrahigh-efficiency thermal rectification via topological transition of photonic density of states and near-field radiation gap variations, *ACS Photon.* **11**, 1271 (2024).
- [104] K. Ito, A. Miura, H. Iizuka, and H. Toshiyoshi, Parallel-plate submicron gap formed by micromachined low-density pillars for near-field radiative heat transfer, *Appl. Phys. Lett.* **106**, 083504 (2015).
- [105] J. I. Watjen, B. Zhao, and Z. M. Zhang, Near-field radiative heat transfer between doped-Si parallel plates separated by a spacing down to 200 nm, *Appl. Phys. Lett.* **109**, 203112 (2016).
- [106] J. DeSutter, L. Tang, and M. Francoeur, A near-field radiative heat transfer device, *Nat. Nanotechnol.* **14**, 751 (2019).
- [107] R. Messina and M. Antezza, Scattering-matrix approach to Casimir-Lifshitz force and heat transfer out of thermal equilibrium between arbitrary bodies, *Phys. Rev. A* **84**, 042102 (2011).
- [108] I. Latella, P. Ben-Abdallah, S.-A. Biehs, M. Antezza, and R. Messina, Radiative heat transfer and nonequilibrium

- Casimir-Lifshitz force in many-body systems with planar geometry, *Phys. Rev. B* **95**, 205404 (2017).
- [109] I. Latella, S.-A. Biehs, R. Messina, A. W. Rodriguez, and P. Ben-Abdallah, Ballistic near-field heat transport in dense many-body systems, *Phys. Rev. B* **97**, 035423 (2018).
- [110] S.-A. Biehs, R. Messina, P. S. Venkataram, A. W. Rodriguez, J. C. Cuevas, and P. Ben-Abdallah, Near-field radiative heat transfer in many-body systems, *Rev. Mod. Phys.* **93**, 025009 (2021).
- [111] M. Auslender and S. Hava, Scattering-matrix propagation algorithm in full-vectorial optics of multilayer grating structures, *Opt. Lett.* **21**, 1765 (1996).
- [112] J. Drevillon, Design ab-initio de matériaux micro et nanostructurés pour l'émission thermique cohérente en champ proche et en champ lointain, Ph.D. thesis, Université de Nantes (2007).
- [113] P. Yeh and M. Hendry, Optical waves in layered media, *Phys. Today* **43**, 77 (1990).